Building Archean cratonic roots

Charitra Jain[1,2], Antoine B. Rozel[3], Jeroen van Hunen[1], Emily J. Chin[4], and Antonio Manjón-Cabeza Córdoba[3,5]

[1]Department of Earth Sciences, Durham University, Durham, United Kingdom
[2]GFZ German Research Centre for Geosciences, Section of Geodynamic Modelling, Potsdam, Germany
[3]Institute of Geophysics, Department of Earth Sciences, ETH Zurich, Zurich, Switzerland
[4]Scripps Institution of Oceanography, UC San Diego, La Jolla, United States
[5]Instituto Andaluz de Ciencias de la Tierra (IACT), UGR-CSIC, Armilla, Spain

Correspondence: Charitra Jain (charitrajaingeo@gmail.com)

Abstract.

Geophysical, geochemical, and geological investigations have attributed the stable behaviour of Earth's continents to the presence of their Archean cratonic roots. These roots are likely composed of melt-depleted, low density residual peridotite with high Magnesium number (Mg#), while devolatilisation from the upper mantle during magmatic events might have made these roots more viscous and intrinsically stronger than the convecting mantle.

Several conceptual dynamic and petrological models of craton formation have been proposed. Dynamic models invoke far-field shortening or mantle melting events, e.g., by mantle plumes, to create melt-depleted and thick cratons. Compositional buoyancy and rheological modifications have also been invoked to create long-lived stable cratonic lithosphere. However, these conceptual models have not been tested in a dynamically self-consistent model. In this study, we present global thermochemical models of craton formation with coupled core-mantle-crust evolution driven entirely by gravitational forces.

Our results with melting and crustal production (both oceanic and continental) show that formation of cratonic roots can occur through naturally occurring lateral compression and thickening of the lithosphere in a self-consistent manner, without the need to invoke far-field tectonic forces. Plume impingements, and gravitational sliding creates thrusting of lithosphere to form thick, stable, and strong lithosphere that has a strong resemblance to the Archean cratons that we can still observe today at the Earth's surface. These models also suggest the recycling of denser eclogitic crust by delamination and dripping processes.

Within our computed parameter space, a variety of tectonic regimes are observed which also transition with time. Based on these results, we propose that a ridge-only regime or a sluggish-stagnant-lid regime might have been active on Earth during the Archean Eon as they offer favourable dynamics and conditions for craton formation.

1 Introduction

The relative stability and longevity of Earth's continents compared to its ephemeral oceanic crust are attributed to the presence of cratons, which are regions of continental lithosphere that have resisted deformation for several billion years. Cratons are underlain by cold and thick mantle roots (Pearson et al., 2021), which can extend up to several hundreds of kms deep as evidenced by xenolith P-T data (Lee et al., 2011) and observations of low surface heat flux (Nyblade, 1999; Pollack et al.,

1993) and high seismic velocities (Jordan, 1979; Grand and Helmberger, 1984). These roots are generally considered to be composed of residual peridotites, which can be classified into fertile lherzolitic (primitive mantle or pyrolytic) and highly melt-depleted harzburgitic lithologies (Boyd, 1987, 1989). It has been proposed that progressive melt extraction from the igneous protolith increases the magnesium number Mg# in these residues, thereby decreasing their densities (Jordan, 1979; Lee, 2003; Schutt and Lesher, 2006). On average, cratonic mantle is cooler than the ambient mantle, which would result in a density increase owing to thermal contraction. Jordan (1978, 1988) proposed that under perfectly isopycnic conditions, the positive compositional buoyancy emanating from these residual peridotites would exactly offset the negative thermal buoyancy of the colder cratonic mantle. However, having this net neutral buoyancy may not be enough to ensure cratonic stability. Pollack (1986) argued that devolatilisation from the upper mantle during magmatic events elevates the solidus of the residual mantle making it more refractory and stiff, thereby making it less susceptible to subsequent melting and entrainment in the convecting mantle. Geological record suggests that the efficiency of devolatilisation and partial melting have decreased over time in response to the secular cooling of the mantle (Herzberg et al., 2010). Since then, experimental results have shown a substantial reduction in the viscosity of olivine in the presence of water (Hirth and Kohlstedt, 1996). Volatiles are highly incompatible in solids during melting, and therefore it has been hypothesised that cratonic roots are made of melt-depleted and dehydrated peridotites, which are considerably more viscous and intrinsically stronger than the convecting mantle (Hirth et al., 2000; Lee et al., 2011).

The mechanisms behind the formation and stabilisation of these cratonic roots, however, remain debated (Pearson et al., 2021) and three separate hypotheses have been proposed with each having their strengths and caveats (Pearson and Wittig, 2008; Lee et al., 2011). One model involves high degrees of melting within a large thermal plume (Herzberg, 1993; Griffin et al., 2003; Griffin and O'Reilly, 2007; Arndt et al., 2009) leaving behind a melt-depleted, dehydrated, and low-density residue, which would explain the higher viscosity and the buoyancy observed in the roots. This model predicts an increase in peridotite fertility (low melt-depletion and Mg#) with depth as higher amounts of melt would be extracted at shallower depths during decompression melting. However, such gradual chemical stratification has not been widely observed in cratons (Lee et al., 2011). The plume model also fails to explain the subsolidus history of pressure increase experienced by the cratonic peridotites (Lee and Chin, 2014). Another model involves underthrusting or stacking of subducted oceanic lithosphere (Helmstaedt and Schulze, 1989; Canil, 2004, 2008; Simon et al., 2007; Pearson and Wittig, 2008) which could explain the low-pressure protoliths of cratonic peridotites and the lack of compositional stratification with depth, but it also has several drawbacks. The negatively buoyant oceanic lithosphere is more likely to subduct than stack (Arndt et al., 2009), unless the downgoing plate is captured (Saleeby, 2003; Luffi et al., 2009) Large-scale weak zones or fault planes in the supposedly stronger continental mantle might have been necessary for imbrication of oceanic lithosphere to work. Lee et al. (2008) proposed that serpentinisation of the oceanic mantle during the mid-Archean to the early Proterozoic might have provided the weak zones. Furthermore, a mechanism is needed to remove the eclogite from the oceanic lithosphere as the predicted amount is inconsistent with its rare presence among the mantle xenoliths in kimberlites (Schulze, 1989). The third model involves making cratonic roots by accretion and thickening of already buoyant arc lithosphere (Şengör et al., 1993; Ducea and Saleeby, 1998; Kelemen et al., 1998; Parman, 2004), which might have been active during the Phanerozoic. For this mechanism to work, the arc has to be

mature enough to be in a compressional state and arc magmatism has to coincide with lithospheric thickening (DeCelles et al., 2009; Kay et al., 2005). Despite the presence of some similarities between rocks from modern continental arcs and Precambrian xenoliths, this mechanism needs further validation by integrating field data with geochemical and petrological studies (Lee et al., 2011).

Wang et al. (2018) explored the viability of compressive thickening models to make cratonic roots in their numerical experiments. They presented a two-stage growth model, in which a tectonic shortening stage of the residual mantle for 10s of Myr is followed by gravitational self-thickening stage that lasts for 100s of Myr. The authors further showed that the long-term secular cooling of the mantle prevents a Rayleigh-Taylor type collapse and helps with cratonic root preservation. Beall et al. (2018) proposed that a rapid transition from heat-pipe dominated vertical tectonics to plate tectonics during the Archean might have provided stresses high enough to thicken the cratonic lithosphere. The authors initialised their lid-breaking model with a buoyant and strong layer that undergoes compression and stabilises. Recently, models by Perchuk et al. (2020) showed oceanic subduction followed by arc-continent collision under Archean conditions. Using a prescribed convergence rate, they demonstrated protokeel formation by viscous underplating of the low-density, melt-depleted sublithospheric oceanic mantle during subduction, which subsequently matures into keels with conductive cooling. Capitanio et al. (2020) showed the formation of cratonic lithospheric mantle by melt-depletion induced dehydration stiffening beneath a long-lived stretching lid. Over time, these regions stiffen, resist deformation and force strain migration and cooling.

Besides formation, the preservation and stability of cratonic roots until present-day has also been studied. Previous numerical modelling work has shown that the positive chemical buoyancy of the cratonic lithosphere is not enough to keep it from entraining into the underlying convecting mantle (Lenardic and Moresi, 1999; Lenardic et al., 2003; Sleep, 2003). Using scaling analysis and considering a weakly temperature-dependent viscosity, Sleep (2003) showed that a viscosity increase of a factor 20 between the cratonic lithosphere and the ambient mantle would help with the craton survival. Lenardic et al. (2003) proposed that high cratonic root viscosity only helps stabilising the cratonic lithosphere when its thickness is twice larger than that of the oceanic lithosphere. Additionally, having higher brittle yield stress in the cratonic lithosphere or the presence of mobile belts (weak zones) around cratons also helps with cratonic root stability. O'Neill et al. (2008) further showed cratonic stability in their models having a compositional viscosity ratio of 50-150 between the root and the asthenosphere along with a root/oceanic lithospheric yield stress ratio of 5-30. The authors also argued that hotter Archean mantle temperatures would result in lower viscosities and reduced stresses around cratons, thereby promoting cratonic survival. Using simulations with non-Newtonian rheology, Wang et al. (2014) showed resistance of compositionally buoyant cratonic roots against erosion by small scale convection for billion year timescales when initialised with a strengthening viscosity factor of 3 in the rheological prefactor, leading to an effective viscosity increase of about 50 (3^n, with $n = 3.5$) when accounting for the non-Newtonian contribution. They also reported that for cratonic roots with no intrinsic buoyancy, a higher strengthening factor on the order of 10 leading to an effective viscosity contrast of over a thousand is required to ensure their stability.

Even though models have been instrumental in testing the validity of different geological and geophysical hypotheses, there are either regional scale or upper-mantle models and thus by design, lack mantle plumes and convective activity offered by global models, as well as a self-regulating thermal evolution. Extending the previous work by Jain et al. (2019), in this study,

we present whole mantle convection models that are capable of generating cratons in a self-consistent manner, i.e., without any artificial forcing of surface velocities. Furthermore, we test whether lithospheric compression and tectonic thickening can occur naturally in our models and aid with the formation of cratonic roots.

2 Physical Model and Numerical Model

To investigate how Earth built cratonic roots in a self-consistent way, we model its thermochemical evolution during the Archean Eon (4.0-2.5 Ga) with realistic parameter values (Table 1) suited for early Earth conditions. The model includes pressure-, temperature-, and water-dependent viscosity, plasticity, time-dependent radiogenic and basal heating, phase transitions, and melting leading to basaltic and felsic crust production. We introduce a temperature-, pressure-, and composition-dependent solubility function, which controls the water ingassing and outgassing. Moreover, we improve upon the existing melting parameterisation of Jain et al. (2019) by making the solidi and liquidi depend on water saturation and introduce Magnesium number (Mg#) evolution.

2.1 Conservation Equations, Boundary Conditions, and Solution Method

We use the code StagYY (Tackley, 2008) to solve the compressible anelastic convection equations in a two-dimensional spherical annulus geometry (Hernlund and Tackley, 2008). StagYY employs a Eulerian mesh with radial refinement on which equations for momentum conservation, continuity and heat diffusion/production are solved using the finite volume approach. The computational domain considered here is quadrant annulus, where the grid is divided into 512 (laterally) times 128 (radially) cells. Additionally, ~ 1.3 million Lagrangian tracers, carrying various quantities (see below), are advected in the computational domain. Free slip boundary conditions are used at the core-mantle boundary and the surface. Side boundary conditions are periodic.

The Stokes equation is given by

$$0 = -\nabla P + \nabla \cdot \tau + \rho \mathbf{g}, \tag{1}$$

where P is pressure, τ is the stress tensor, ρ is the density, and $\mathbf{g}$ is the gravitational acceleration, which has a homogeneous magnitude. Density is computed as a function of pressure, temperature, and composition including solid-solid phase transitions, following a 3rd order Birch-Murnaghan equation of state (Tackley et al., 2013).

The continuity equation is given by:

$$\nabla \cdot (\rho \mathbf{u}) = 0, \tag{2}$$

where $\mathbf{u}$ is the velocity vector.

The advection-diffusion equation is given by:

$$\rho C_P \left(\frac{\partial T}{\partial t} + \mathbf{u} \cdot \nabla T \right) - \alpha T \left(\mathbf{u} \cdot \nabla P \right) = \nabla \cdot (k \nabla T) + \tau : \nabla \mathbf{u} + \rho H, \tag{3}$$

where C_p is the heat capacity, T is temperature, α is the thermal expansivity, k is the conductivity and H is the radiogenic heating. The terms on the right hand side are calculated on the mesh, whereas advection and adiabatic temperature changes are performed on the tracer level. Only the changes in the temperature field (as opposed to the temperature itself) due to the right hand side terms are interpolated to the tracers at each time step to limit numerical diffusion.

Tracers are advected in the flow using velocities interpolated from the cell edges, where the Stokes and continuity equations (Eqs. 1 and 2) are solved together with a direct PETSc solver (Balay et al., 2012) and Picard iterations of the viscosity. . We found that a second order interpolation and a fourth order Runge-Kutta scheme is necessary to prevent gaps from opening in the tracer field. Tracers carry various quantities such as temperature, composition, water, radiogenic heating, time of melting, etc. Tracers are also transported instantly, when magmatism occurs, through the procedure detailed in section 2.4.

The surface temperature (300 K) is kept constant whereas the core-mantle boundary (CMB) temperature (4500 K) evolves using the model proposed by (Buffett et al., 1992, 1996), allowing for the cooling due to the CMB heat flux and taking into account the energy necessary to grow the inner core (for parameterisation details, see (Nakagawa and Tackley, 2004)).

2.2 Rheology

A visco-plastic rheology is considered where the viscous deformation is accommodated by grain-size independent diffusion creep. The mantle is divided into 3 different layers i: upper mantle (1), lower mantle (2) and post-perovskite layer (3), with each layer having different values for activation energy E_i and activation volume V_i (Karato and Wu, 1993; Yamazaki and Karato, 2001). Following the Arrhenius law, the temperature-, pressure-, and water- dependent viscosity is given as (see Table 1 for constants):

$$\eta(T,P,w) = \eta_0 \Delta\eta_i A_w \exp\left(\frac{E_i + PV_i}{RT} - \frac{E_i}{RT_0}\right), \tag{4}$$

where η_0 is the reference viscosity at zero pressure and reference temperature T_0 (1600 K), $\Delta\eta_i$ is the viscosity offset between layer i and the reference viscosity, A_w is the water-dependent viscosity multiplicative factor, P is the pressure, R is the gas constant and T is the absolute temperature. η_0 is valid for the phase system olivine and the reference composition ('pyrolite' as explained in Section 2.3), both of which have viscosity multipliers of 1 (see Table 1). The activation volume decreases exponentially with increasing pressure in each layer i according to the relation:

$$V(P) = V_i \exp\left(-\frac{P}{P_i}\right). \tag{5}$$

where P_i is the pressure scale which is different for each layer i as given in Table 1. Based on the experimental data and assuming that the activation parameters are independent of the water content (Karato, 2015), the presence of water modulates the viscosity by factor A_w as:

$$A_w = \left[\Delta\eta_w + (1-\Delta\eta_w)\left(\frac{C_w}{C_{w0}}\right)^{r_w}\right]^{-1}, \tag{6}$$

where $\Delta\eta_w$ is the viscosity offset due to water (or dehydration strengthening), C_w is the cell water concentration, C_{w0} is the reference water concentration (100 ppm), and $r_w = 1$. In this work, the viscosity of the material drier and wetter than

100 ppm are increased and decreased respectively. However, for water concentrations higher than 100 ppm, the weakening would be the same irrespective of $\Delta\eta_w$. Further viscosity jumps of 10 and 0.1 are applied at the upper-lower mantle transition (660 km) (Čížková et al., 2012) and perovskite-post-perovskite transition (2740 km) (Hunt et al., 2009; Ammann et al., 2010) respectively.

To allow for plastic deformation in the lithosphere, plastic yielding is assumed (Moresi and Solomatov, 1998; Tackley, 2000). The maximum stress that a material can sustain before deforming plastically is given by the yield stress σ_{Y}, which has both brittle and ductile components:

$$\sigma_{\mathrm{Y}} = \min\left(\sigma_{\mathrm{Y,ductile}}, \sigma_{\mathrm{Y,brittle}}\right). \tag{7}$$

The ductile yield stress $\sigma_{\mathrm{Y,ductile}}$ increases linearly with pressure as:

$$\sigma_{\mathrm{Y,ductile}} = \sigma_{\mathrm{Y}}^{0} + \acute{\sigma_{\mathrm{Y}}} P, \tag{8}$$

where σ_{Y}^{0} is the surface ductile yield stress and $\sigma_{\mathrm{Y}}^{\prime}$ is the pressure gradient of the ductile yield stress. Following Byerlee (1978), the brittle yield stress $\sigma_{\mathrm{Y,brittle}}$ is calculated as:

$$\sigma_{\mathrm{Y,brittle}} = \mu P, \tag{9}$$

where μ is the friction coefficient. If the convective stresses exceed the yield stress, the viscosity is reduced to the yielding viscosity $\eta_{\mathrm{Y}} = \sigma_{\mathrm{Y}}/2\dot{\epsilon}$, where $\dot{\epsilon}$ is the 2nd invariant of the strain-rate tensor. The effective viscosity is then given by:

$$\eta_{\mathrm{eff}} = \left(\frac{1}{\eta} + \frac{2\dot{\varepsilon}}{\sigma_{\mathrm{Y}}}\right)^{-1}. \tag{10}$$

To mitigate large viscosity variations and ensure code stability, viscosity limiters are applied. On the lower end, viscosity is limited to 10^{18} Pa·s. For the upper end, different values are used in this study. All simulations considered a reference viscosity $\eta_0 = 10^{20}$ Pa·s and initial mantle potential temperature $T_{\mathrm{P0}} = 1900$ K. Additionally, melt-depletion induced density reduction of the residual harzburgite (peridotite) is considered implicitly by including phase changes (see Section 2.3 for details). The simulations start at 4.0 Ga (or 4 Gyr before present-day) as the evolution during the Hadean Eon (4.5-4.0 Ga) is not considered. Time is running forward from 0-1500 Myr and it represents the Archean Eon (4.0-2.5 Ga). Accordingly, the radioactive elements are initialised with concentrations, which are appropriate for the period.

2.3 Phase Changes and Composition

The model uses a parameterisation based on mineral physics data (Irifune and Ringwood, 1993; Ono et al., 2001), in which the mantle materials are divided into olivine (ol), pyroxene-garnet (px-gt), TTG, and melt phase systems. Solid-solid phase transitions are assumed within the olivine and pyroxene-garnet phase systems as considered previously in Xie and Tackley (2004); Nakagawa and Tackley (2012). The composition is mapped linearly into the fraction of different phase systems and it can either be in the continuum between end-members, *harzburgite* (ultramafic and depleted material, 75% ol and 25% px-gt)

Table 1. Non-dimensional and dimensional parameters along with the rheological properties for 3 different layers i used in this study (UM = Upper Mantle (dry olivine); PV = Perovskite; PPV = Post-Perovskite)

Property	**Symbol**	**Value**	**Units**
Initial internal heating rate	H	18.77×10^{-12}	W/kg
Radiogenic half-life	t_{half}	2.43	Gyr
Ductile yield stress gradient	σ'_{Y}	0.01	-
Reference viscosity	η_0	1×10^{20}	Pa·s
Surface temperature	T_{surf}	300	K
Initial potential temperature	T_{P0}	1900	K
Eruption efficiency	e	30	%
Gas constant	R	8.3145	J/K/mol
Gravitational acceleration	g	9.81	m/s^2
Mantle thickness	D	2890	km
Specific heat capacity of pyrolite	$C_{P,\text{pyr}}$	1200	J/kg/K
Specific heat capacity of basalt	$C_{P,\text{bas}}$	1000	J/kg/K
Specific heat capacity of TTG	$C_{P,\text{TTG}}$	1000	J/kg/K
Latent heat of pyrolite	L_{pyr}	600	kJ/kg
Latent heat of basalt	L_{bas}	380	kJ/kg
Latent heat of TTG	L_{TTG}	300	kJ/kg
Surface thermal expansivity^s	α	3×10^{-5}	K^{-1}
Surface thermal conductivity^s	k	3.5	W/m/K
Activation energy - UM	E_1	300	kJ/mol
Activation volume - UM	V_1	5.00	cm^3/mol
Pressure scale - UM	P_1	∞	GPa
Viscosity multiplier - UM	$\Delta\eta_1$	1.0	-
Activation energy - PV	E_2	370	kJ/mol
Activation volume - PV	V_2	3.65	cm^3/mol
Pressure scale - PV	P_2	200	GPa
Viscosity multiplier - PV	$\Delta\eta_2$	30.0	-
Activation energy - PPV	E_3	162	kJ/mol
Activation volume - PPV	V_3	1.40	cm^3/mol
Pressure scale - PPV	P_3	1610	GPa
Viscosity multiplier - PPV	$\Delta\eta_3$	0.1	-

^{s} valid at the surface for olivine phase system.

Table 2. Phase change parameters for olivine, pyroxene-garnet, and TTG systems with surface density at zero pressure ρ_s, density jump across a phase transition $\Delta\rho$, and Clapeyron slope γ.

Depth (km)	Temperature (K)	$\Delta\rho$ (kg/m^3)	γ (MPa/K)
Olivine ($\rho_s = 3240$ kg/m^3)			
410	1600	180	2.5
660	1900	400	-2.5
2740	2300	61.6	10
Pyroxene-Garnet ($\rho_s = 3080$ kg/m^3)			
40	1000	350	0
400	1600	150	1
720	1900	400	1
2740	2300	61.6	10
TTG ($\rho_s = 2700$ kg/m^3)			
290[a]	1713	168	2.26

and *basalt* (mafic igneous rocks, 100% px-gt), or *TTG* (felsic rocks). The mantle is initialised with a pyrolytic composition: 80% harzburgite and 20% basalt (Xu et al., 2008), thus being a mixture of 60% olivine and 40% pyroxene-garnet. At a depth of 40 km, a basalt-eclogite phase transition is applied which makes basalt denser than harzburgite by around 190 kg/m^3 and has a first-order influence on the lithospheric dynamics (Lourenço et al., 2016). At a depth of 290 km, TTG material undergoes a coesite-stishovite phase transition (Akimoto and Syono, 1969; Akaogi and Navrotsky, 1984; Gerya et al., 2004) and its density increases by 168 kg/m^3. Additionally, in the deeper mantle, the phase transition to post-perovskite is considered (e.g. Tackley et al. (2013)). The phase change parameters are given in Table 2. Changes in composition arise from melt-induced differentiation, which is described in the next section.

2.4 Melting and Crustal Production

We used the melting model initially developed by Xie and Tackley (2004); Nakagawa et al. (2010), and further extended by Jain et al. (2019) for self-consistent generation of oceanic and continental crust by two-step mantle differentiation. Any newly generated melt is partly intruded at the base of the pre-existing crust as molten material and partly erupted at the surface as solid crust. The mass ratio of erupted to intruded material follows a specified constant value of 30:70 (corresponding to 30 % eruption efficiency) based on the previous studies by Rozel et al. (2017); Jain et al. (2019), which have demonstrated the important role of intrusive-dominated magmatism towards producing Archean TTG rocks. In this study, we introduce a solubility function and use solidi that are hydration- and composition- dependent.

2.4.1 Hydration- and composition- dependent solidi

In this study, 8 pressure-dependent solidus temperatures corresponding to 4 compositions (harzburgite, pyrolite, basalt and TTG) and for both hydrated and dry conditions are pre-computed (presented in Fig. A1a and Table A1). The solidus temperature used in the melting routines are interpolated from these pre-computed quantities, instead of being extrapolated from the pyrolite solidus. Specific P-T windows (Moyen, 2011) have been previously used to estimate TTG volumes (Rozel et al., 2017) or to form TTGs (Jain et al., 2019), yet a given range of melt fraction itself was not required. Using interpolated solidi, the TTG windows are matched with a realistic melt fraction as the hydrated solidus for basalt is well controlled and extrapolation-related problems are avoided. Once the end members' solidi are known, the solidus of material of any composition and hydration is obtained via a three step procedure: (1) calculation of the cell water saturation, and (2) interpolation of end-member solidus in the water saturation space, and (3) interpolation of the solidus in the composition space (if required). The detailed parameterisation is given in Appendix A.

2.5 Water ingassing, partitioning, outgassing and solubility

In our simulations, water is a prerequisite for formation of TTG rocks and its concentration has a direct influence on the rheology, when dehydration strengthening is considered. At each time-step, the surface rocks in the top 10 km are saturated with water based on the solubility function (ingassing). Like other quantities such as radionuclides or trace elements, water is partitioned during melting and/or solidification with a partitioning coefficient $D_p = 0.01$. This ensures that the majority of water present in overheated hydrated rocks (i.e., when the temperature exceeds the solidus) is partitioned into the newly formed melt. When the melt is erupted/intruded, water is also transported along with it, thereby removing water from larger depths (outgassing). Furthermore, to account for the limited water storage capacity of the mantle, a temperature-pressure-composition-dependent saturation limit, i.e., solubility is imposed, above which water is instantaneously transported upwards. Fig. 1 depicts the solubility of water (in weight %) of each compositional end-member as a function of temperature and pressure. The bottom row shows the water solubility calculated in hydrous minerals with Perplex (Connolly, 2009). The top row shows the approximated solubility that is employed in our simulations to minimise possible extrapolation artefacts. Note that the water solubility in solids is only non-negligible at low temperature and high pressure. Therefore only cold downwellings can possibly bring water into the transition zone. The analytical functions used to calculate the approximated solubility are described in Appendix B.

2.6 Magnesium number

The parameterisation for magnesium number (Mg#) employed here is based on the previously proposed empirical relationships obtained by studying experimental melts coexisting with olivine and orthopyroxene. Lee and Chin (2014) identified protolith P-T of 1-5 GPa and 1400-1750 °C for cratonic peridotites and proposed that building blocks for cratonic material were generated by hot shallow melting. The parameterisation details are given in Appendix C.

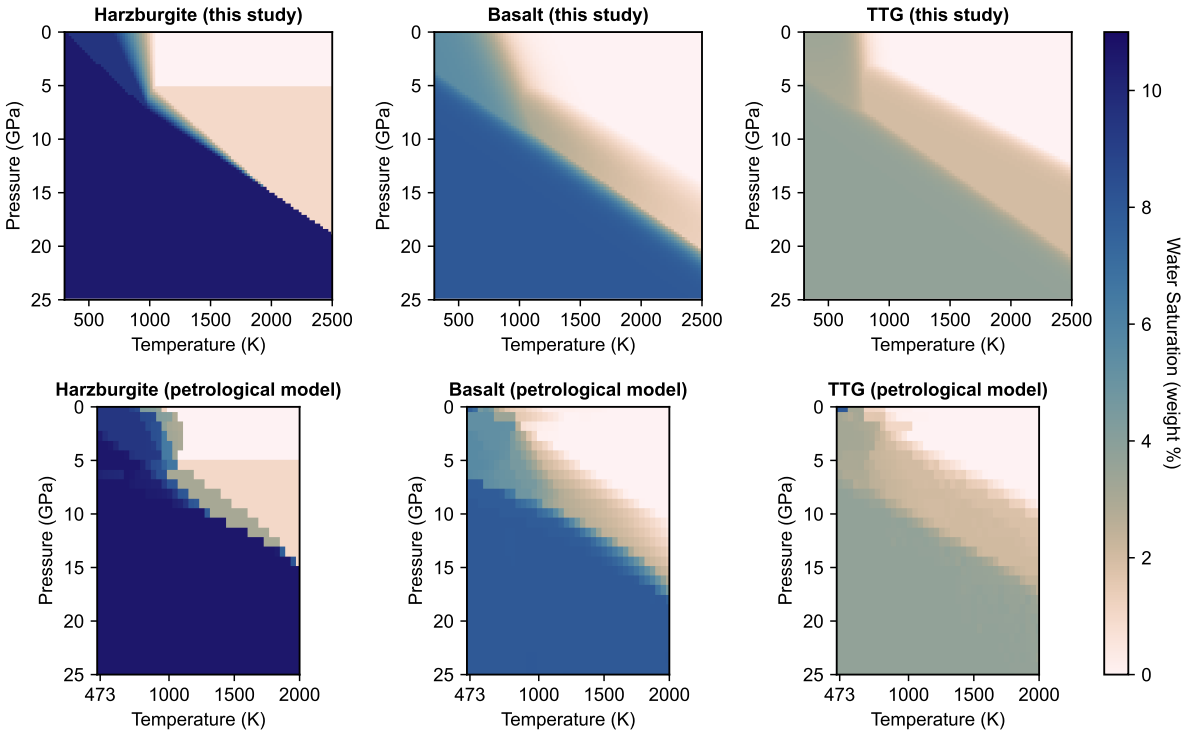

Figure 1. Water solubility maps. Top row: analytical functions used in our models. Bottom row: look-up tables obtained with Perplex (Connolly, 2009).

3 Results

First, two representative simulations (A13 and B8) are shown (compositional evolution illustrated in Figs. 2, 3) to highlight the variety of processes and conditions that can lead to the formation of cratons. Following that, a parameter sensitivity study is presented and the influence of different model parameters elucidated.

3.1 Simulation A13

Fig. 2 illustrates the evolution of a typical simulation with a relatively high lithospheric strength, hereafter referred to as simulation A13. Early decompression melting events caused by mantle plumes result in widespread crust formation. The residual mantle material becomes depleted and has a higher harzburgite content. The newly generated basaltic melt is partly intruded at the base of the pre-existing crust as molten material and partly erupted at the surface as solid oceanic crust, following an eruption efficiency of 30 %. Within each cell, the oceanic crust melts to generate TTG melt, provided that water solubility in basalt exceeds 50% and the necessary P-T conditions for TTG formation Moyen (2011) are met. Following the same eruption

efficiency, a fraction of this melt solidifies at the surface as felsic crust, while the rest is intruded at the bottom of felsic crust (if pre-existing) as molten material.

As the primary goal of this work is to understand the processes that lead to craton formation, relevant material properties are continuously tracked and visualised. Since cratonic roots are understood to be viscous, buoyant, depleted, and dehydrated, the cratonic roots in this work are represented with lithosphere older than 750 Myr with a Mg# > 0.905, and water concentration between 10-50 ppm (unless otherwise noted). The age of the mantle considered here is based on the last time the material underwent melting. By definition, any material is only considered as cratonic root if it has been around for more than 750 Myr, and therefore cratonic roots only appear during the later stages of the model evolution.

The mantle plumes are the major driver behind the lithospheric dynamics and tectonic regimes observed here. For the first $\sim$250 Myr, the intense plume activity generates crust and recycles it by means of negatively buoyant subducting slabs. The dynamics observed here are similar to mobile-lid (ML) regime (Stein et al., 2004; Tackley, 2000), which is often reported in numerical models as an equivalent of plate tectonics where oceanic lithosphere descends into the mantle. From 250 Myr onwards, as plumes reach the surface, they push away the lithosphere laterally in both directions at a spreading ridge, which can be seen as a discrete zone of divergence in the velocity field in Fig. 2.

The compression of the pre-existing oceanic and continental crust leads to the tectonic shortening and thickening along horizontal and vertical axes respectively. Around 900 Myr, the cratonic roots start to appear and get thickened and buried deeper with the ongoing compression. The thickened oceanic crust undergoes an eclogite phase transition and is 190 kg/m^3 denser than the surrounding residual mantle. This dense lithosphere is gravitationally unstable and its lower layers start to delaminate and drip into the lower mantle. Over time, an accumulation of this recycled oceanic crust can be seen at the core-mantle boundary. During 250-1500 Myr, the ridge continues to spread and no new subduction zones develop. These dynamics persist for a long time and could be considered identical to processes shown by models that exhibit a ridge-only (RO) regime (Rozel et al., 2015). Fig. 4 illustrates these shifts in tectonic regimes observed in our models.

3.2 Simulation B8

Fig. 3 illustrates the evolution of a simulation with dehydration strengthening and moderate lithospheric strength, hereafter referred to as simulation B8. Similar to A13, B8 shows two-stage mantle differentiation and the formation of both oceanic and continental crust. The plumes are driving the lithospheric compression and tectonic thickening, however, without forming any subduction zones or ridges. Non-yielding lithosphere is covering the entire surface (seen as the viscous lid in Fig. 5), akin to stagnant-lid (SL) regime (Christensen, 1984; Solomatov, 1995). However, the lithosphere is still deforming internally and therefore the simulation is classified as a "sluggish-stagnant-lid" (SSL) regime throughout its evolution. Around 1000 Myr, the cratonic roots start to appear and by 1300 Myr, the underthrusting of oceanic crust is seen as a result of the ongoing natural lithospheric compression. Similar stacking of subducted oceanic lithosphere has been suggested to have taken place in the Kimberley block of the Kaapvaal craton during the Neoarchean (Pearson and Wittig, 2008). Furthermore, this model shows that the excess eclogite (expected as a result of stacking) from the cratonic roots can be efficiently removed with the

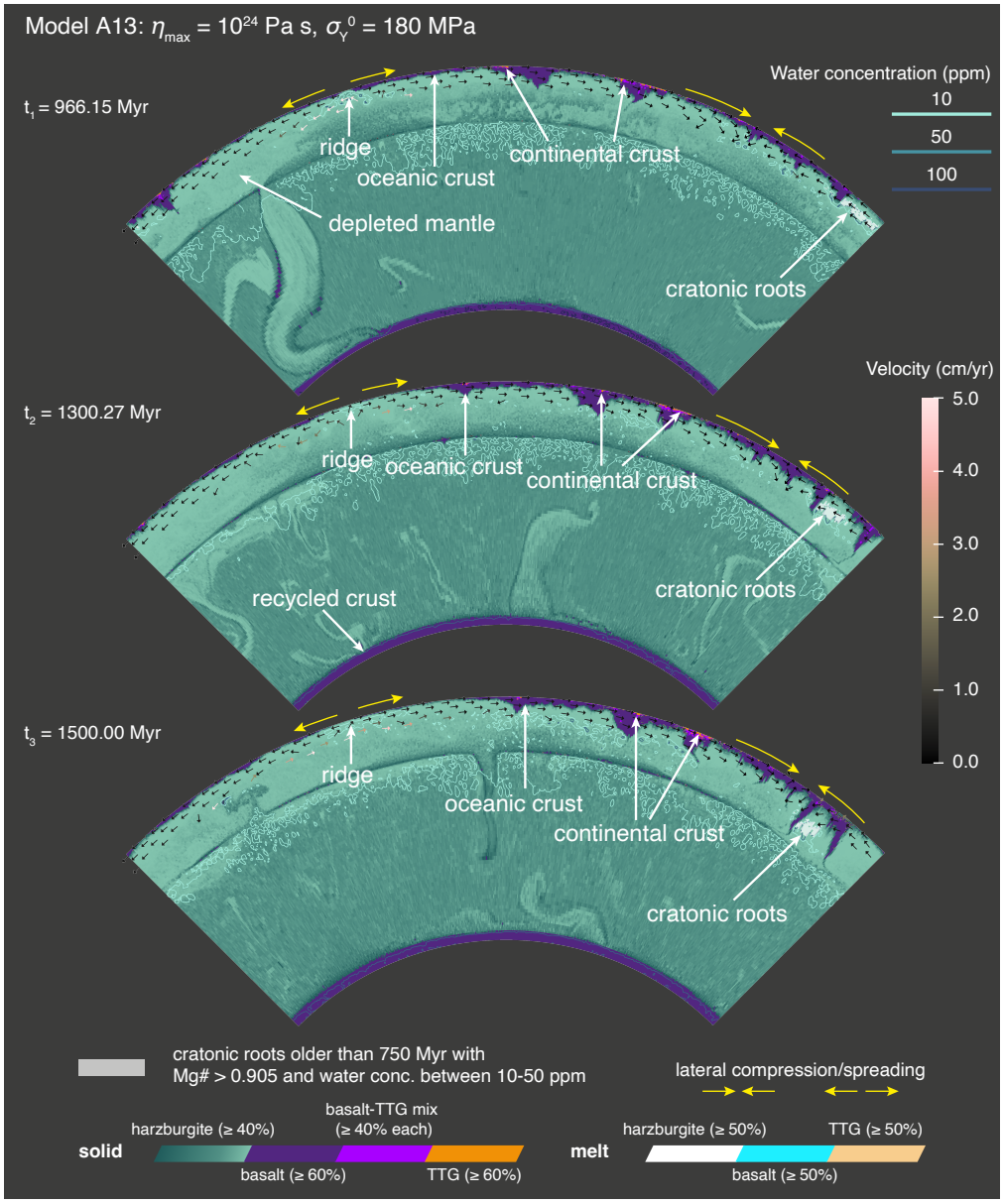

Figure 2. Compositional evolution with time of simulation A13 showing the formation of cratonic roots (grey shaded regions). The individual cells may contain more than one material at a given time, and therefore a threshold of minimum local concentration for each material is employed for their visualisation. Cell-based composition field has the following solid and molten materials: *TTG* ($\geq$ 60% in tangerine), *basalt* ($\geq$ 60% in dark purple), *harzburgite* ($\geq$ 40% in teal, lighter shades represent higher harzburgite content and mantle depletion), *TTG-melt* ($\geq$ 50% in peach-orange), *basaltic-melt* ($\geq$ 50% in sky blue), *harzburgitic-melt* ($\geq$ 50% in white), and *TTG-basalt-mix* ($\geq$ 40% *TTG* and $\geq$ 40% *basalt* in light purple). Superimposed are the contours for water concentration and velocity arrows in the lithosphere.

delamination and dripping processes. Animated versions of model simulations A13 and B8 are available as supplementary material.

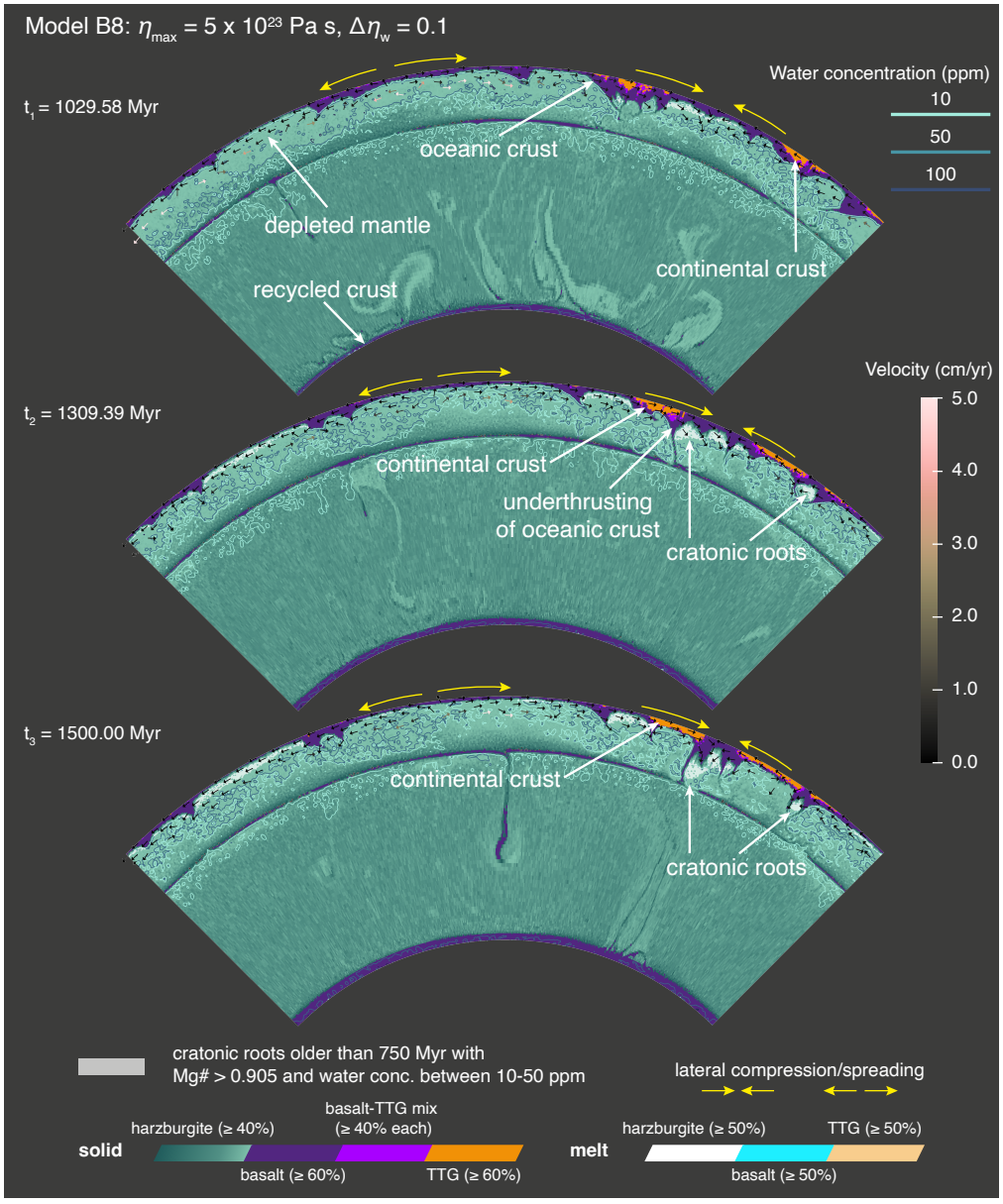

Figure 3. Compositional evolution with time of simulation B8 in its later stages showing the formation of cratonic roots (grey shaded regions). Superimposed are the contours for water concentration and velocity arrows in the lithosphere. The reader is referred to Fig. 2 caption for explanation of different composition fields.

3.3 Influence of model parameters

Important, but poorly constrained rheological parameters that significantly affect the mantle and lithosphere dynamics in these models are lithospheric strength and the influence of fluids on the material strength. Therefore, we explored the rheological parameter space that is spanned by three key model parameters: lithospheric strength (denoted by maximum viscosity limiter η_{max}), plastic yielding (denoted by surface ductile yield stress σ_{Y}^{0}), and dehydration strengthening (denoted by viscosity offset due to water $\Delta\eta_w$). To independently assess the parameter sensitivity towards cratonic formation and stability, a total of 38 simulations were performed, which can be categorised in three different sets presented in Fig. 4. For each simulation considered in the parameter space, Fig. 4 shows the temporal evolution of its tectonic regime and whether it forms cratonic roots or not. Initially, the lithospheric strength is varied in conjunction with either plastic yielding (set A) or dehydration strengthening (set B). Building upon these results, all three parameters are varied simultaneously (set C). To illustrate the variety of tectonic regimes observed across all the model simulations, Fig. 5 shows a compilation of those. For a selection of cases from the parameter space, Fig. 6 shows the temporal evolution of mean mantle temperature, surface root-mean-square (rms) velocities, crustal volume (basaltic and felsic) and TTG mass.

3.3.1 Set A

Simulations with $\eta_{\text{max}} = 10^{23}$ Pa·s do not grow a lithosphere strong enough to resist any deformation. There is naturally occurring tectonic shortening and thickening of the crustal material, however, the crust is being continuously generated and recycled into the mantle due to the plume activity. The cold downwellings are efficient in cooling down the mantle and surface rms velocities remain on the order of several cm/year (curve A1 in Fig. 6A,B). Higher values of σ_{Y}^{0} (180/240/300 MPa) push the brittle-ductile transition to greater depths and change the recycling mechanism. This is evident from simulations A1-A5 where the tectonic regime shifts from a mobile-lid (ML) to a plutonic-squishly-lid (PSL). With higher σ_{Y}^{0}, the lithosphere can thicken more before it deforms plastically in a ductile manner. While simulations with a ML regime have negatively buoyant oceanic lithosphere subducting as long, thin, and coherent slabs (several 1000s of km scale), the simulations with a PSL regime are characterised by short, thick, and ephemeral plates (several 100s of km scale). Once transformed into the denser eclogitic material at a depth of 40 km, the thicker lithosphere becomes gravitationally unstable and starts to drip and delaminate (see Fig. 5 for visual comparison of different tectonic regimes). Simulations with $\eta_{\text{max}} = 5 \times 10^{23}$ Pa·s also show crustal shortening and thickening while exhibiting a variety of tectonic regimes depending on σ_{Y}^{0}. However, no stable continents form as most crust is recycled by either global- or regional-scale resurfacing events. For instance, A7 shows an episodic-lid (EPL) regime, where the entire lithosphere resurfaces over a period of 200-300 Myr. It can be considered as a form of unstable stagnant-lid (SL) regime and has been proposed to be active on Venus (Armann and Tackley, 2012; Moresi and Solomatov, 1998; Noack et al., 2012; Turcotte, 1993). This resurfacing can be seen as a decline in mean mantle temperature or a spike in surface rms velocity around 800 Myr in Fig. 6A,B. The crustal volume fluctuates highly as the recycled crust melts again to generate new basaltic and felsic crust (Fig. 6C). In cases with $\eta_{\text{max}} = 10^{24}$ Pa·s, lower σ_{Y}^{0} values (60/120 MPa) result in a stagnant-lid (SL) regime covering the entire surface (Fig. 4). Lithospheric erosion from underneath happens but the lithosphere (single lid) doesn't yield or compacts

laterally. These cases have many downwellings in the initial stages (ML in the first ~ 250 Myr) triggered by plumes and the mantle cools down drastically. The colder mantle convects less vigorously and causes less deformation. With higher σ_Y^0 values (180/240/300 MPa), the planet exhibits a RO regime and forms cratonic roots, albeit with occasional global resurfacing events. For instance, with no major downwellings, case A13 shows a steady increase in mean mantle temperature and the surface rms velocity remains below 1 cm/yr (Fig. 6A,B).

3.3.2 Set B

Simulations with $\eta_{\max} = 10^{23}$ Pa·s have shortening of crustal (TTG+basaltic) material and are in a PSL regime. While the denser basaltic-eclogitic crust recycles into the mantle, a high proportion of the buoyant TTG crust remains preserved at the surface (compare B5 curve in panels **C)** and **D)** of Fig. 6). On the way down, the downwellings release water, which accumulates in the transition zone. Following the imposed saturation limits (see Section 2.5 for details), this water migrates upwards, thereby hydrating the asthenosphere and reducing its viscosity by the offset $\Delta\eta_w$. As a result of tectonic shortening, there is underthrusting of the old and depleted lithosphere beneath the TTG crust. However, these stacked domains have water concentrations reaching up to 5000 ppm and hence are not classified as cratonic roots in this study. Cases with $\eta_{\max} = 10^{24}$ Pa·s show tectonic shortening and thickening and are in a SSL regime. Crustal recycling is minimal and only happens in the form of eclogitic drips (see curve B12 in panels **C)** and **D)** of Fig. 6). As a result, the overall thicker crust retains most of the water and the underlying upper mantle is drier and stronger when compared to cases with $\eta_{\max} = 10^{23}$ Pa·s. There is some stacking of depleted lithosphere, leading to formation of cratonic roots. However, excess eclogite remains in these depleted domains. The mean mantle temperature continues to rise and surface rms velocities remain low (see curve B12 in panels **A)** and **B)** of Fig. 6). Cases with an intermediate value $\eta_{\max} = 5 \times 10^{23}$ Pa·s show crustal recycling which is somewhat higher than cases with $\eta_{\max} = 10^{24}$ Pa·s (compare curves B8 and B12 in Fig. 6C). All these cases demonstrate the successful formation of cratonic roots by underthrusting mechanism while efficiently removing excess eclogite from the cratonic roots.

3.3.3 Set C

Based on the absence of cratonic roots from the relevant simulations of sets A and B, the value of $\eta_{\max} = 10^{23}$ Pa·s was dropped from further numerical experiments. All cases start with a PSL as high σ_Y^0 values push the brittle-ductile transition deeper into the upper mantle. Post-arrival of the first plumes at the surface, simulations exhibit different tectonic regimes depending on the parameters chosen. Most cases with $\eta_{\max} = 5 \times 10^{23}$ Pa·s (C1-C3) show a SL at different onset times with a single lid covering the entire surface. Prior to that, a RO regime operates as long as a high lithosphere-asthenosphere viscosity contrast exists. The higher amount of water in the asthenosphere (brought down with recycled oceanic crust) weakens the material and accentuates this viscosity contrast. For instance, a global resurfacing event shifts the tectonic regime from a RO to a SL for case C1 around 380 Myr. A correlation between a sudden drop in mean mantle temperature, a spike in surface rms velocities, and decrease in crustal volume is evident from Fig. 6. C4 shows underthrusting and formation of cratonic roots, only if the criterion of maximum water concentration allowed is relaxed from 50 ppm to 200 ppm. All cases with $\eta_{\max} = 10^{24}$ Pa·s (C5-C8) show lithospheric compression and thickening. Viscous and depleted cratonic roots also form, once the maximum water concentration allowed

is increased to 200 ppm. Irrespective of the σ_Y^0 value employed, the dynamics and tectonics depend more on the value of $\Delta\eta_w$. With a lower value of $\Delta\eta_w = 0.1$, cases C5 and C7 are operating in RO regime. With a higher value of $\Delta\eta_w = 0.01$, cases C6 and C8 are exhibiting SSL. What differentiates C6 and C8 from B15 is that with the combination of plasticity and dehydration strengthening, the entire lithosphere is old and viscous as opposed to localised cratonic root formation underneath or around continental margins.

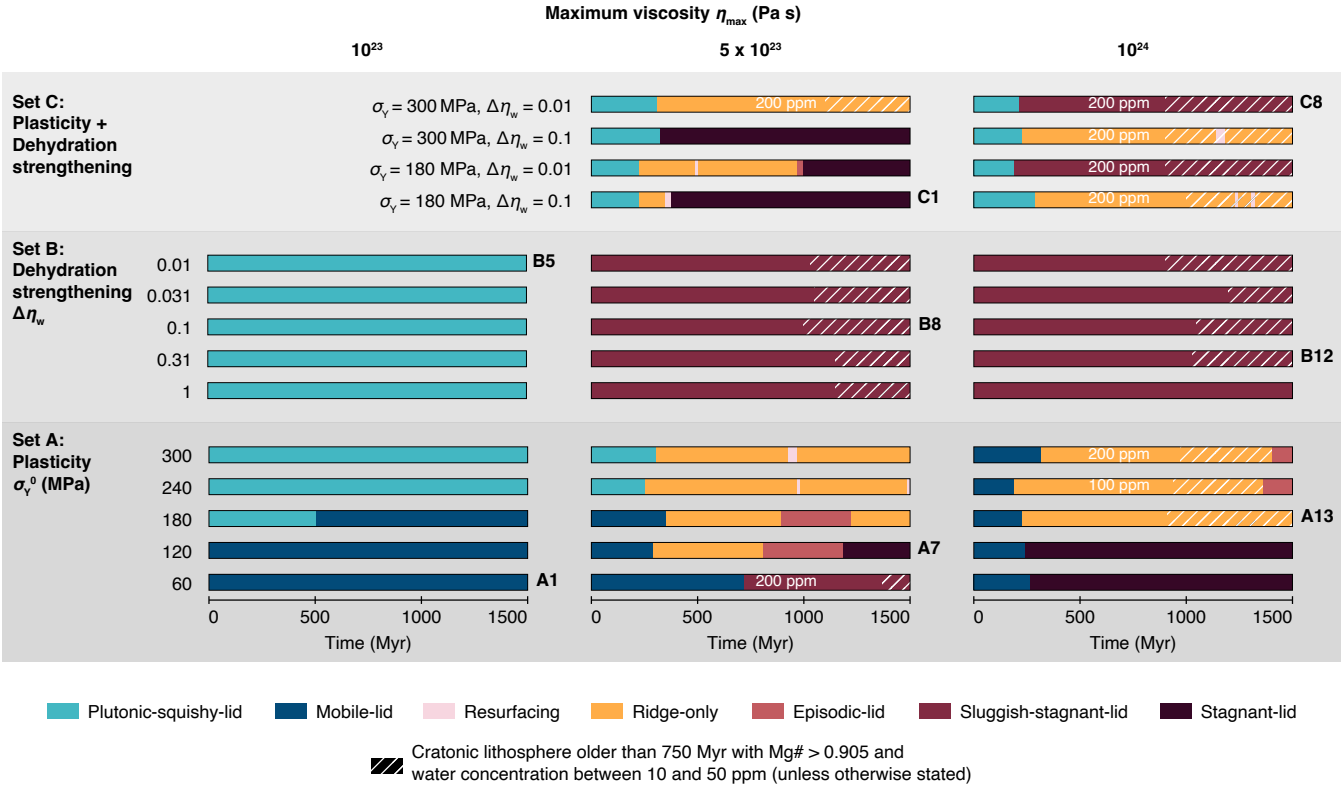

Figure 4. Temporal evolution of different tectonic regimes for the entire parameter space. Also highlighted are the cases, which have cratonic roots.

4 Discussion

4.1 Formation of cratonic roots and their defining criteria

As introduced in Section 1, several hypotheses have been proposed to explain the origin of cratons. While the models presented in this study lack the many complexities of a natural system, they are able to form cratonic roots through processes, which could be considered as a combination of different formation mechanisms. In our global models, mantle plumes cause decompression

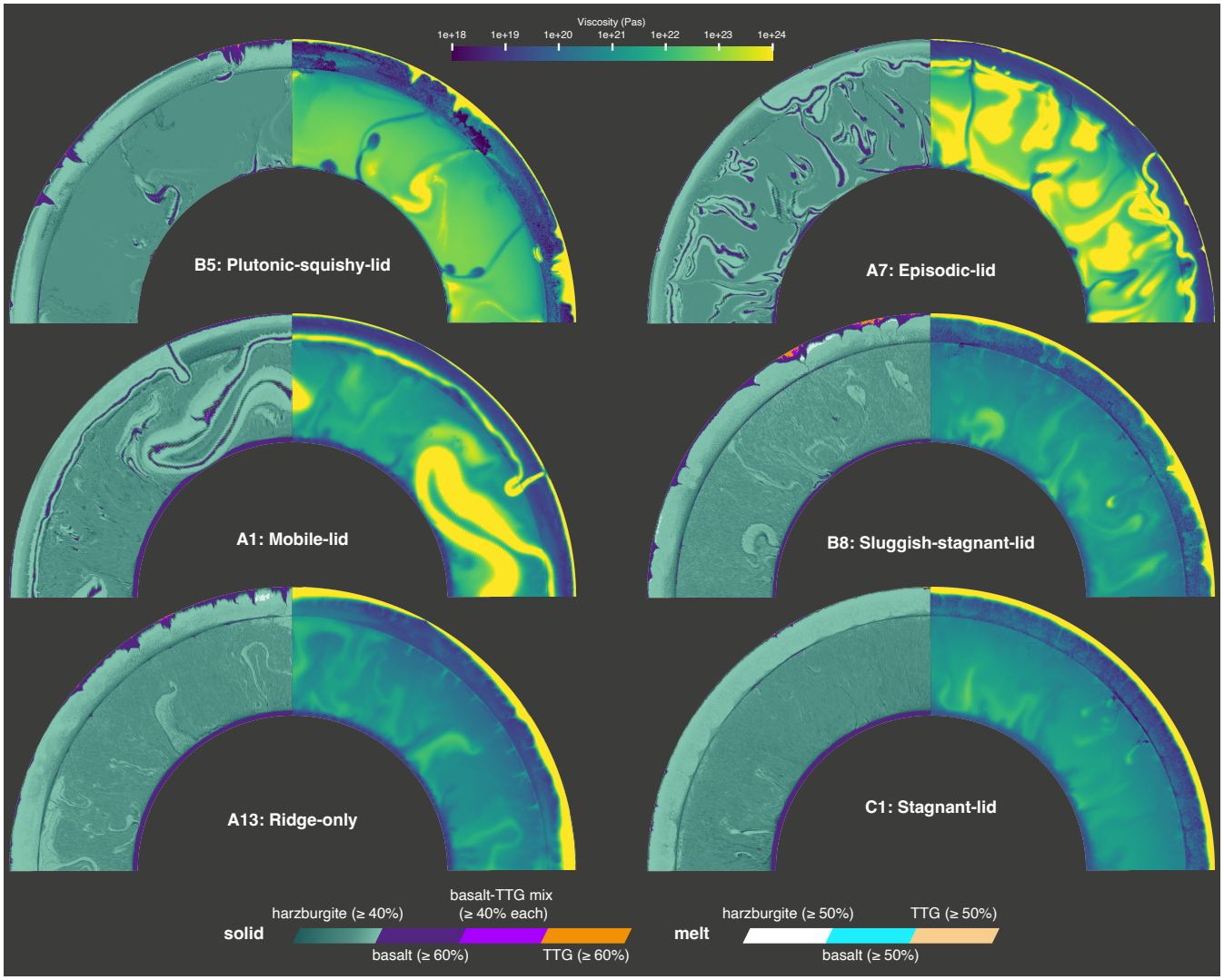

Figure 5. Snapshots of different cases showing composition and viscosity fields to illustrate the different tectonic regimes. Note that, even though different η_{max} values were used in these cases, only one colorscale for viscosity field is shown.

melting and generate continental crust by a two-step mantle differentiation. At the same time, the residual material left in the underlying lithosphere is melt-depleted and dehydrated, but it is not as such considered as cratonic lithosphere in this study. Here, one of the defining criteria for cratonic roots is that the lithosphere has to show resistance against possible erosion or deformation by the convecting mantle for more than 750 Myr., i.e., the material didn't go undergo any further melting. In these models, mantle plumes also cause lithospheric compression, which in turn thickens the lithosphere and facilitates the recycling of gravitationally unstable eclogitic material from the deeper layers. Such cases show processes similar to underthrusting of pre-existing oceanic lithosphere beneath the crust. These processes have been proposed as a formation mechanism (Helmstaedt

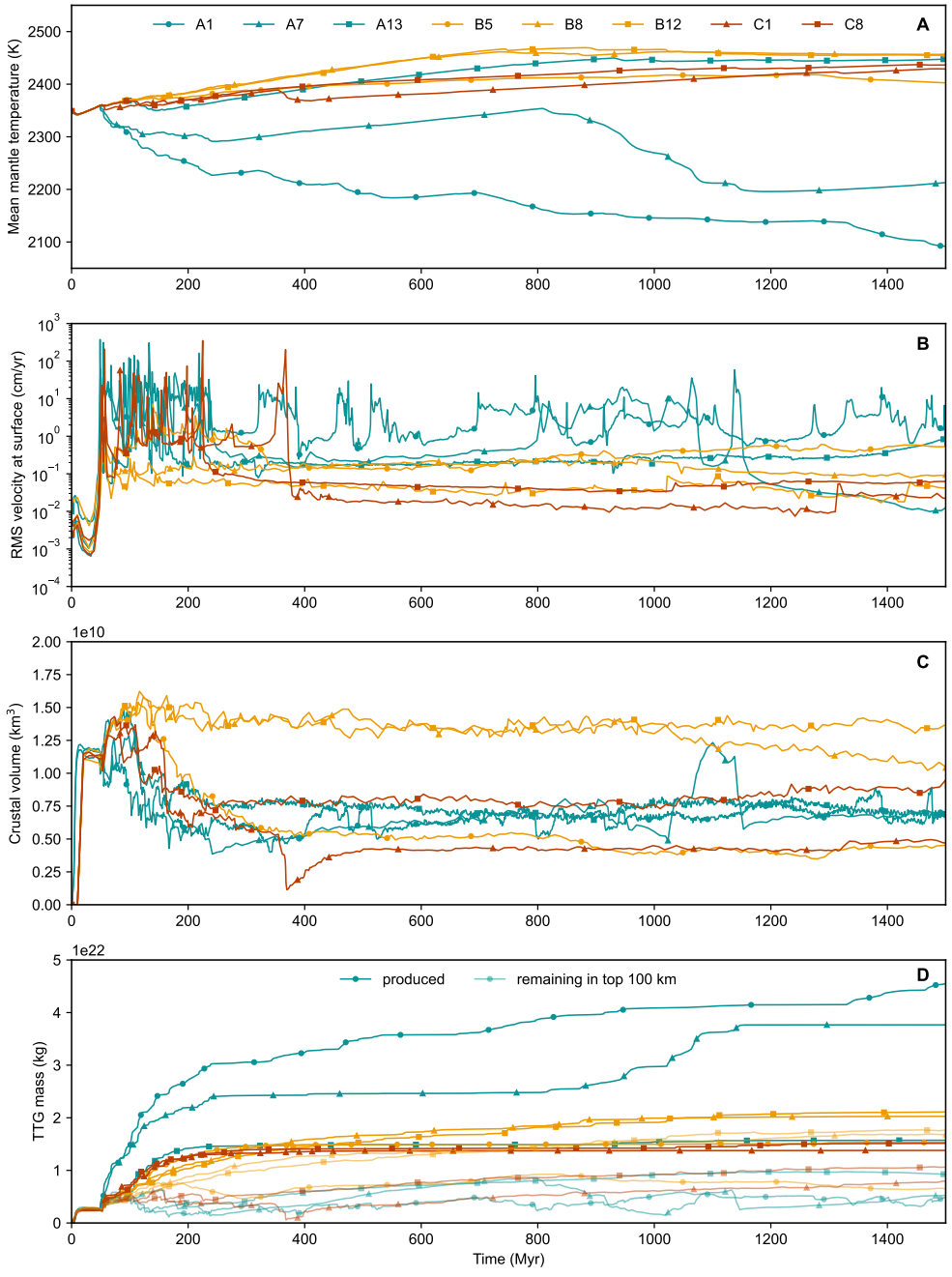

Figure 6. A) Mean mantle temperature, **B)** surface rms velocities, **C)** total crustal volume (basaltic and felsic), and **D)** TTG mass for a selection of cases from the parameter space.

and Schulze, 1989; Canil, 2004, 2008; Simon et al., 2007; Pearson and Wittig, 2008) and might have also been responsible for the pressure increase experienced by cratonic peridotites Lee and Chin (2014).

Cratonic roots are considered to be made of residual peridotites (harzburgite in this study), which are left behind as a result of melting of igneous protoliths (pyrolite in this study). Progressive melt extraction increases the Magnesium number (Mg#) in these residues and makes them compositionally buoyant by decreasing their densities (Boyd, 1987, 1989; Jordan, 1979; Lee, 2003; Schutt and Lesher, 2006). Assumed to be reflective of the secular cooling of the Earth's mantle, Archean peridotites have higher Mg# (0.91-0.94) than Proterozoic and Phanerozoic peridotites (0.90-0.92) (Griffin et al., 2003; Lee et al., 2011). Here, the Mg# evolution during protolith to residual peridotite melting is parameterised using the empirical relationships proposed by Lee and Chin (2014). However, the density reduction of the residual material is not explicitly incorporated (e.g., Lee, 2003). The density decreases implicitly with melt depletion, i.e., with increase in olivine content as a result of the phase changes considered in Section 2.3. As olivine is less dense than pyroxene-garnet below the eclogitic phase transition depth of 40 km, the residual peridotite or harzburgite (75% olivine, 25% pyroxene-garnet) becomes less dense than pyrolite (60% olivine, 40% pyroxene-garnet) below that depth. Accordingly, in this study, another criterion for classifying depleted lithosphere as cratonic roots, is that it must have a Mg# of at least 0.905.

Being intrinsically stronger than the convecting mantle, cratonic roots are understood to be dehydrated with low water concentrations. The amount of water bound in peridotites varies with their age and tectonic environment. The clinopyroxenes from Kaapvaal peridotite xenoliths have water concentrations reaching up to to 400 ppm (Grant et al., 2007; Peslier, 2010), corresponding to 2-18 ppm H_2O content in olivine. The H_2O content of olivine in the MORB mantle source is estimated to be around 10-30 ppm (Hirschmann, 2006). In comparison, clinopyroxenes from the Archean North China Archean and Proterozoic Colorado Plateau are drier and wetter respectively (Yang et al., 2008; Li et al., 2008). As the most depleted mantle material (harzburgite) in these simulations only has 75% olivine (the rest being pyroxene-garnet), a water concentration of 10-50 ppm is considered as another defining criteria for cratonic roots. For some cases, this upper limit of 50 ppm is relaxed to 100 or 200 ppm.

4.2 Tectonic regimes during the Archean and their implications

For the early Earth, post magma ocean solidification (Abe, 1993a,b, 1997; Elkins-Tanton, 2012), a variety of tectonic regimes, such as heat-pipe tectonics (Moore and Webb, 2014), plume-lid tectonics (regional-scale) (Sizova et al., 2010; Fischer and Gerya, 2016a,b) or plutonic-squishy-lid (global-scale) (Lourenço et al., 2020), stagnant-lid (Debaille et al., 2013) have been proposed albeit without any consensus. And when it comes to narrowing down the onset of subduction-driven plate tectonics, opinions vary widely with a multitude of studies proposing its inception anytime between the Hadean Eon (4.5-4.0 Ga) and the Neoproterozoic Era (1.0-0.54Ga) (Korenaga, 2013; Palin and Santosh, 2020). While the main objective of this study was to model self-consistent craton formation, the simulations presented here also offer us a diversity of tectonic regimes. These modelling results, therefore, allow us to discuss the possible operation and implications of these following different regimes on Archean Earth with respect to formation of cratonic roots. PSL in our numerical models is characterised by having a thin lithosphere, small and ephemeral plates, surface rms velocities around 10 cm/yr and crustal recycling in the form of thick

blocks of delaminated and dripping material. Modelled ML has negatively buoyant oceanic lithosphere going down as thin and coherent slabs and surface rms velocities can reach up to 100 cm/yr in the first 200 Myr. In models with a RO regime, a discrete zone of divergence forms in the lithosphere without the presence of any subduction zones. Previously, this regime has been suggested to operate on early Earth by Tackley (2000); Rozel et al. (2015) where they employed a depth-dependent yield stress in their models. At the spreading ridge, the lithosphere is pushed laterally in both directions, resulting in its compaction and thickening. One of the main goals of this study was to test whether lithospheric compression and tectonic thickening can occur naturally and help with the formation of cratonic roots, and cases with a RO regime are successful in doing that. But the lower layers of this thickened lithosphere are made of dense eclogitic material. In some cases (A7, A8, A14, A15), these dense layers reach a thickness of several 100 kms. The resulting lithosphere is gravitationally unstable and delaminates over a period of 200-300 Myr. Along with the delaminated lithosphere, the cratonic roots also get entrained and recycled. Although, the time period of these global resurfacing events is a magnitude higher than what has been reported before (Lourenço et al., 2016), these events are still classified as a characteristic of EPL regime in this study.

Another difference in our definition of EPL regime is that these resurfacing events happen following the RO regime, unlike the classical definition of EPL, where SL precedes the overturns/resurfacings. Some cases also exhibit a SL regime where the entire surface is covered by a single-lid as the lithosphere doesn't yield and there is no lateral compression or tectonic thickening. As cratons are understood to be regions of crustal basement localised underneath continental crust, this single-lid is not considered as cratonic lithosphere in this study. Finally, there are cases with SSL regime that make cratonic roots. These cases show lithospheric compaction and tectonic thickening as well as underthrusting of oceanic crust, which is one of the proposed mechanisms in literature to make cratonic roots.

Based on these results of coupled core-mantle-crust evolution on global scale, we propose the following shifts in tectonic regimes during Earth's early history. In the Hadean, with the higher core temperature, mantle plumes must have been stronger and responsible for the majority of the crust production and recycling. Assuming that most of the magmatism on early Earth was dominated by plutonism (Rozel et al., 2017; Jain et al., 2019; Lourenço et al., 2020) similar to present-day (Crisp, 1984), PSL on a global scale or plume-lid tectonics on a regional scale might have been operational. During the Archean, the rapid cooling of the core and the resulting less efficient crustal recycling might have ensured that the majority of the water is retained in the crust itself. The underlying mantle would have been melt-depleted, strong, and relatively dry. Mantle plumes might have facilitated the lateral compaction and the subsequent tectonic thickening of the lithosphere. During this compaction, the stacking of oceanic lithosphere might have led to the formation of stable cratonic roots. And the denser eclogitic material might have then delaminated and dripped into the lower mantle as shown in our models. These dynamics would have been possible under a RO or a SSL regime.

4.3 Felsic crustal volume, recycling, and TTG proportions

The crustal volume and mass of produced TTG are computed after correcting for the geometry used in these simulations (see Appendix D for details). While a big proportion of the felsic crust is produced in the first ~ 250 Myr of the Archean with the arrival of the first mantle plumes, the crustal growth is continuous for the entire 1500 Myr evolution (see Fig. 6C,D). This is

in agreement with the findings of Moyen and Laurent (2018) and Jain et al. (2019). Also visualised is the remaining mass of TTG in the top 100 km, which tells us about the intensity of recycling: very high for cases A1 (ML regime), A17 (RO and EPL regimes) and minimal for B8, B12 (both SSL regime).

Recent work by Guo and Korenaga (2020) also advocates for rapid continental crust growth during the early Earth. The authors modelled Argon degassing with thermal evolution of Earth and estimated that more than 80% of the mass of present-day continental crust was already reached during the Archean. This would correspond to a production of 5×10^{22} kg of felsic rocks during the Archean (Korenaga, 2021). Table E1 lists the cumulative mass of TTG produced, which varies between 1.38×10^{22} - 4.55×10^{22} kg depending on the simulation. The tectonic regime and the subsequent water concentration in the upper mantle has a direct influence on the amount of TTG produced. In cases with a ML regime (A1 for example), recycling of oceanic lithosphere releases water, leading to higher TTG production. In cases with a SSL regime (B12 for example), crustal recycling is minimal and it stores most of the water, thereby resulting in lower TTG production.

Moyen (2011) classified the Archean TTGs into three different types based on the pressure of their formation settings: low-pressure (10-12 kbar), medium-pressure (ca. 15 kbar), and high-pressure (20 kbar or higher) TTGs, which account for 20%, 60%, and 20% of the sodic TTGs, respectively. Using global models, Rozel et al. (2017) estimated TTG volumes and proposed that a plutonism-dominated PSL regime would be able to reproduce this observed proportions of different TTG rocks. However, in a follow-up study, Jain et al. (2019) reported relative proportions of 85%, 14.5%, and 0.5% based on their models of TTG production. In their work, most of the TTGs were produced at the tip of the deformation fronts when plumes spread laterally at the surface. Therefore, these models lacked certain tectonic processes that might have been responsible for the production of high-pressure TTGs. In the present study, the best case scenario for these relative proportions is 65%, 20%, and 15%, which occurs for simulations operating with SSL regime (see Table E1 for all simulations). These simulations show lithospheric compression and tectonic thickening without any subduction zones. This allows the basaltic crust to get buried to higher pressures and results in an increased proportion of high-pressure TTGs.

4.4 Model limitations and possible future improvements

Although these models offer us insights about the formation of stable continents during early Earth, they have certain shortcomings, which should be addressed in future studies. First, these models do not consider grain-size dependent rheology (Bercovici and Ricard, 2005, 2014; Ricard and Bercovici, 2009; Rozel et al., 2011), which might help with the stabilisation of cratonic roots (King, 2005). Hall and Parmentier (2003) showed a viscosity increase in regions of low convective stresses due to grain size evolution. Grains might grow bigger in the low strain environments of cratonic roots and might make them stronger. Second, cratonic roots in our models are not as compositionally buoyant as what is expected from geological observations. Third, Mondal and Korenaga (2018); Korenaga (2021) argue that delamination of the dense, thick, and gravitationally unstable eclogitic crust in our models may not occur if a stronger rheology for eclogite is considered (Jin et al., 2001). Fourth, mantle plumes might have a limited impact on the lithosphere dynamics in 3-D models with opposing effects. On one hand, this might reduce the lithospheric compression and tectonic thickening responsible for the formation of cratonic roots. On the other hand, the stability of already formed cratonic lithosphere might improve. Fifth, increasing the resolution in these global simulations

might allow us to reproduce geological features such as dome and keel structures (Van Kranendonk et al., 2004; Hickman, 2004; Van Kranendonk, 2011). Finally, future work is needed to self-consistently model the regime transition from pre-plate tectonics active during early Earth to subduction-driven plate tectonics.

5 Conclusions

We have presented global mantle convection models that generate viscous, melt-depleted (with Mg# > 0.905), dehydrated (with 10-200 ppm water content), and stable (older than 750 Myr) cratonic roots in a self-consistent manner. We considered the protolith P-T conditions of cratonic peridotites previously identified by Lee and Chin (2014) and modelled the Mg# evolution in the mantle. In our models, formation of cratonic roots happens as a result of a combination of different tectonic processes and for a range of rheological parameters employed in this study. Initially, decompression melting caused by mantle plumes generates oceanic crust and Archean continental crust (TTG rocks). Concurrently, the residual material left behind in the underlying lithosphere is melt-depleted and dehydrated. Over time, this lithosphere gets laterally compacted and thickened and evolves into long-lived and strong cratonic roots. Our simulations show a variety of tectonic regimes and transitions between these regimes over time are also observed. In cases with a ridge-only (RO) regime, there is no active subduction and the lithosphere is laterally compressed on both sides of a long-lasting spreading ridge. Cases with a sluggish-stagnant-lid (SSL) regime also show naturally occurring lateral compression and thickening of the lithosphere, thereby allowing the cratonic roots to mature over 100s of millions of years. Most simulations also show underthrusting of oceanic lithosphere beneath the pre-existing crust, which has been suggested by Pearson and Wittig (2008) to explain the evolution of the Kaapvaal craton during the Neoarchean. The denser eclogitic material within these underthrusted domains is gravitationally unstable and is recycled into the lower mantle by delamination and dripping processes. These simulations, therefore, also offer a mechanism to explain the rare presence of eclogites among the mantle xenoliths in kimberlites (Schulze, 1989). We envisage that early Earth exhibited different tectonic regimes during its evolution. Considering the strong nature of initial mantle plumes, a plutonic-squishy-lid (PSL) regime was active during the Hadean Eon and led to intense production and recycling of both oceanic and continental crust. Sometime during the Archean Eon, the secular cooling of the mantle and the increase in lithospheric rigidity caused a regime transition to a RO or a SSL, which offered conditions suitable for the formation of cratonic roots.

Code availability. The convection code StagYY is the property of P. J. T. and ETH Zurich and is available for collaborative studies from P. J. T. (paul.tackley@erdw.ethz.ch). The scripts and raw datasets used to produce Figures 1 and 6 for this study can be downloaded from Zenodo with the following DOI: 10.5281/zenodo.6630970.

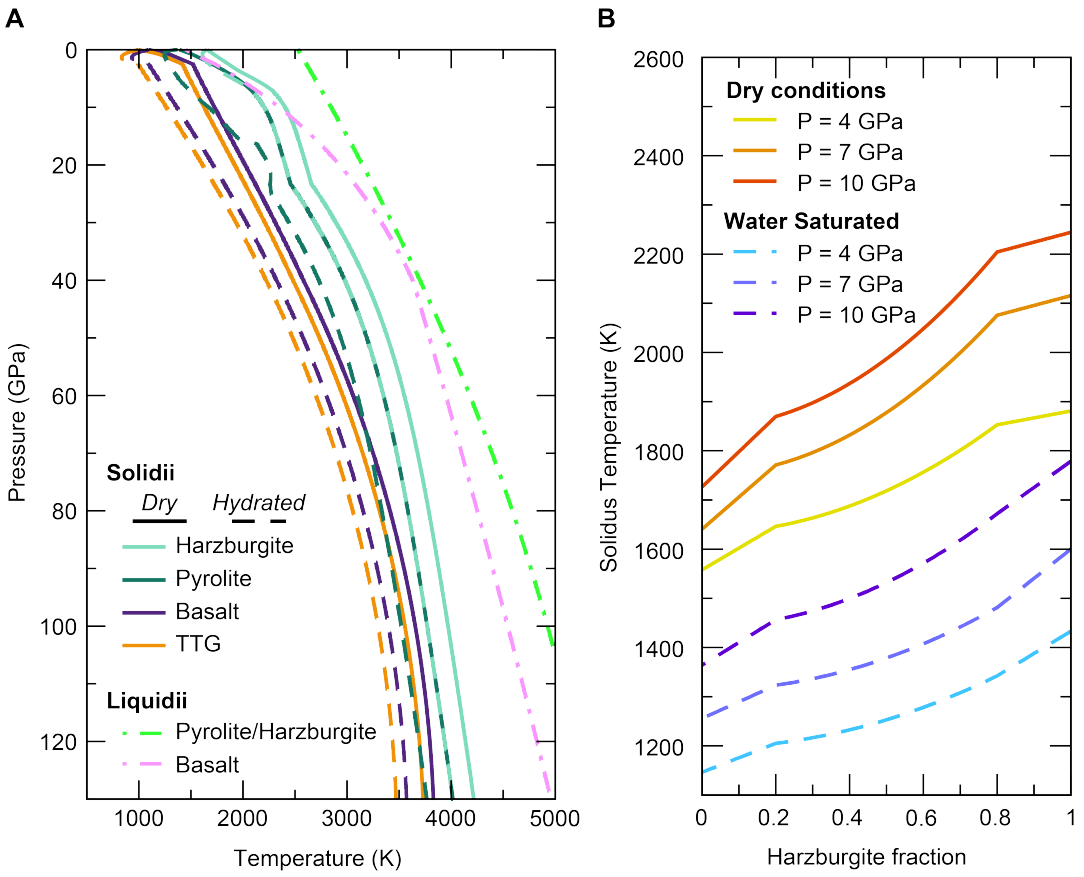

Figure A1. A) Solidus and liquidus temperature profiles, **B)** Solidus temperatures as a function of composition.

Appendix A: Interpolated solidi and melt fraction

The average water saturation w_s of each cell is obtained by mass averaging the compositional groups:

$$w_s = \sum_i w_{s,i} x_i \tag{A1}$$

where x_i represents the mass fraction of the entity i in the cell and $w_{s,i}$ is the saturation of water. i can represent: (1) solid basalt/eclogite which has previously erupted or intruded, (2) molten basalt/eclogite which has previously erupted or intruded, (3) solid basalt/eclogite possibly mixed with harzburgite which has not erupted/intruded before, (4) molten basalt/eclogite possibly mixed with harzburgite which has not erupted/intruded before, (5) solid TTG, (6) molten TTG. The hydration-dependent solidus of any end-member composition j (harzburgite "Hz", pyrolite "Pyr", basalt/eclogite "Bs", or TTG) is obtained by

non-linear interpolation in the saturation space:

$$T_{\text{sol,j}}(w_s) = T_{\text{sol,j,dry}} - (T_{\text{sol,j,dry}} - T_{\text{sol,j,wet}}) \left[w_s - 0.15 \left(1 - \left(\frac{w_s - 0.5}{0.5} \right)^2 \right) \right]. \tag{A2}$$

Next, the final solidus is obtained by interpolation in the composition space. We first define solidus temperatures $T_{\text{sol,Bs-Pyr}}(w_s)$ and $T_{\text{sol,Pyr-Hz}}(w_s)$ as:

$$T_{\text{sol,Bs-Pyr}}(w_s) = T_{\text{sol,Bs}}(w_s) + 0.3\,(T_{\text{sol,Pyr}}(w_s) - T_{\text{sol,Bs}}(w_s))\,, \tag{A3}$$

$$T_{\text{sol,Pyr-Hz}}(w_s) = T_{\text{sol,Pyr}}(w_s) + 0.2\,(T_{\text{sol,Hz}}(w_s) - T_{\text{sol,Pyr}}(w_s))\,. \tag{A4}$$

which correspond to key compositions:

$$c_{\text{Bs-Pyr}} = 0.2\,(1 - c_{\text{Bs,ref}})\,, \tag{A5}$$

$$c_{\text{Pyr-Hz}} = 1 - 0.3\,c_{\text{Bs,ref}} \tag{A6}$$

where $c_{\text{Bs,ref}}$ is the fraction of basalt in undifferentiated material and is set to 0.2. Finally, the solidus temperature $T_{\text{sol}}(c_i, w_s)$ of each compositional group is obtained using:

$$T_{\text{sol}} = T_{\text{sol,Bs}}(w_s) + (T_{\text{sol,Bs-Pyr}}(w_s) - T_{\text{sol,Bs}}(w_s))\,\frac{c_{\text{Hz}}}{c_{\text{Bs-Pyr}}} \quad \text{if } c_{\text{Hz}} < c_{\text{Bs-Pyr}} \tag{A7}$$

$$T_{\text{sol}} = T_{\text{sol,Bs-Pyr}}(w_s) + (T_{\text{sol,Pyr}}(w_s) - T_{\text{sol,Bs-Pyr}}(w_s)) \left(\Delta c_1 + 0.15 \left[\left(\frac{\Delta c_1 - 0.5}{0.5} \right)^2 - 1 \right] \right) \quad \text{if } c_{\text{Bs-Pyr}} < c_{\text{Hz}} < (1 - c_{\text{Bs,ref}}) \tag{A8}$$

$$T_{\text{sol}} = T_{\text{sol,Pyr}}(w_s) + (T_{\text{sol,Pyr-Hz}}(w_s) - T_{\text{sol,Pyr}}(w_s))\,\Delta c_2 \quad \text{if } (1 - c_{\text{Bs,ref}}) < c_{\text{Hz}} < c_{\text{Pyr-Hz}} \tag{A9}$$

$$T_{\text{sol}} = T_{\text{sol,Pyr-Hz}}(w_s) + (T_{\text{sol,Hz}}(w_s) - T_{\text{sol,Pyr-Hz}}(w_s))\,\Delta c_3 \quad \text{if } c_{\text{Pyr-Hz}} < c_{\text{Hz}} \tag{A10}$$

where

$$\Delta c_1 = \frac{c_{\text{Hz}} - c_{\text{Bs-Pyr}}}{1 - c_{\text{Bs,ref}} - c_{\text{Bs-Pyr}}} \tag{A11}$$

$$\Delta c_2 = \frac{c_{\text{Hz}} + c_{\text{Bs,ref}} - 1}{c_{\text{Pyr-Hz}} + c_{\text{Bs,ref}} - 1} \tag{A12}$$

$$\Delta c_3 = \frac{c_{\text{Hz}} - c_{\text{Bs-Pyr}}}{1 - c_{\text{Bs-Pyr}}} \tag{A13}$$

Appendix B: Water solubility

The solubility of water is calculated on each tracer using its pressure, temperature and composition. It is obtained by linear interpolation between the solubilities of the compositional end members obtained with the analytical functions given in Table B1. The solubility of water in melts is also given in Table B1. The solubility of water in solids in the lower mantle is considered to be 0.01 weight %.

The water solubility is calculated after the update of the melt fraction in each cell and after advection-diffusion. Each tracer carrying a water content higher than the solubility loses the excess water. The excess water is transferred to both solid and molten tracers located in the cells above. Tracers receiving water are hydrated if they are not already fully saturated and the

Table A1. Solidus and liquidus temperature parameterisations. d is depth (km).

Material	Solidus/Liquidus temperatures	Pressure/Depth	Source
Dry Hz.	$T_{\text{sol,Hz,dry}} = 1653.15 + 82.9P$	$P < 3.5$	Maaløe (2004)
	$T_{\text{sol,Hz,dry}} = \left(1 - \frac{P-3.5}{3.5}\right) + \frac{P-3.5}{3.5}\left(T_{\text{sol,Pyr}} + \Delta T_{\text{sol,Hz-Pyr,Dry}}\right)$	$3.5 \leq P < 7$	Transition
	$T_{\text{sol,Hz,dry}} = T_{\text{sol,Pyr}} + \Delta T_{\text{sol,Hz-Pyr,Dry}}$	$P \geq 7$	Assumption
Hydr. Hz.	$T_{\text{sol,Hz,hydr}} = T_{\text{sol,Hz,dry}} - \Delta T_{\text{sol,Hz,dry-hydr}}\left(1 - \exp\left(-P\right)\right)$		Assumption
Dry Pyr.	$T_{\text{sol,Pyr,dry}} = 2050 + 0.62d + 660(\text{erf}(d/220) - 1)$	$d \leq 600$ km	Using Herzberg et al. (2000)
	$T_{\text{sol,Pyr,dry}} = 4584 + 0.45d + 3000(\text{erf}(d/8000) - 1)$	$d > 600$ km	Using Zerr et al. (1998)
Hydr. Pyr.	$T_1 = 1673.15 + 250\frac{P-10}{4.8}$		
	$T_2 = 1673.15 + 680\frac{P-13.9}{3.6}$		
	$T_3 = 2108.15 + 145\frac{P-15.6}{4.4}$		
	$T_4 = \frac{40}{P+0.2} + 40P + 1173.15$		Using Kessel et al. (2015)
	$T_5 = T_{\text{sol,Pyr,dry}} - \Delta T_{\text{sol,Pyr,dry-hydr}}$		
	$T_{\text{sol,Pyr,hydr}} = T_4$	$P < 5$	
	$T_{\text{sol,Pyr,hydr}} = \left(2 - \frac{P}{5}\right)T_4 + \frac{P-5}{5}\min(\max(T_1,T_2),T_3)$	$5 \leq P < 10$	Transition
	$T_{\text{sol,Pyr,hydr}} = \min(\max(T_1,T_2),T_3)$	$10 \leq P < 20$	Using Litasov and Ohtani (2002)
	$T_{\text{sol,Pyr,hydr}} = \left(5 - \frac{P}{5}\right)\min(\max(T_1,T_2),T_3) + \frac{P-20}{5}T_5$	$20 \leq P < 25$	Transition
	$T_{\text{sol,Pyr,hydr}} = T_5$	$P \geq 25$	Assumption
Dry Bas.	$T_5 = 1193.15 + 130P$		Pertermann and Hirschmann (2003)
	$T_6 = -1.0116\,10^{-12}P^7 + 8.9986\,10^{-10}P^6$		Using Andrault et al. (2014)
	$-2.9466\,10^{-7}P^5 + 4.781\,10^{-5}P^4 - 3.9836\,10^{-3}P^3$		
	$+7.2596\,10^{-3}P^2 + 36.75P + 1257.9$		
	$T_{\text{sol,Bs,dry}} = T_5 - 100\left(1 - \sin\left(\frac{\pi}{2}P\right)\right)$	$P \leq 1$	Trans. to Moyen (2011)
	$T_{\text{sol,Bs,dry}} = T_5$	$1 < P \leq 2.5$	
	$T_{\text{sol,Bs,dry}} = T_6 - 222.5\left(\exp(-5.33\,10^{-2}P) - 0.118\right)$	$2.5 < P \leq 40$	
	$T_{\text{sol,Bs,dry}} = T_6$	$P > 40$	
Hydr. Bas.	$T_7 = 933.15 + 160\left(\frac{P-1.3}{1.3}\right)^2$		Using Moyen (2011)
	$T_8 = 873.15 + 400\left(\frac{P-1.45}{1.1}\right)^2$		Using Moyen (2011)
	$T_{\text{sol,Bs,hydr}} = \max(T_7,T_8)$	$P \leq 2$	Using Moyen (2011)
	$T_{\text{sol,Bs,hydr}} = T_6 - \Delta T_{\text{sol,Bs,dry-hydr}}$	$2 < P \leq 28.38$	Andrault et al. (2014) + offset
	$T_{\text{sol,Bs,hydr}} = T_6$	$P > 28.38$	Assumption
Dry TTG	$T_{\text{sol,TTG,dry}} = T_{\text{sol,Bs,dry}} - 100$		Assumption
Hydr. TTG	$T_{\text{sol,TTG,hydr}} = T_{\text{sol,Bs,hydr}} - 100$		Assumption

Table B1. Analytical functions used to calculate water saturation. Saturation is expressed in weight %, pressure is in GPa, and temperature is in K. PremDepth is a function given in Table B2.

Harzburgite water saturation function
S_l=9.5; S_{max}=10.5; S_{l2}=S_{max}
$P_{\text{cliff}} = \min\left(7\frac{T-300}{650}, 7+8\frac{T-950}{1050}\right)$
$T_l = 700 + \frac{200P}{5}$; $T_{l2} = 950 + \frac{1050(P-7)}{8}$ $T_r = 1050$; $T_{r2} = 1050 + 950\frac{P-5}{10}$
$\begin{cases} S = 0 & \text{if } P < 5 \\ S = 1 & \text{if } P \geq 5 \end{cases}$
$\begin{cases} S_1 = \min\left(\max(S_l - (T-T_l)/(T_r-T_l)S_l, S), S_l\right) & \text{if } T_r \geq T_l \\ S_1 = S & \text{if } T > T_r \\ S_1 = S_r & \text{otherwise} \end{cases}$
$\begin{cases} S_2 = \min\left(\max(S_{l2} - (T-T_{l2})/(T_{r2}-T_{l2})S_{l2}, S), S_{l2}\right) & \text{if } T_{r2} \geq T_{l2} \\ S_2 = S & \text{if } T > T_{r2} \\ S_2 = S_{l2} & \text{otherwise} \end{cases}$
$S = \max\left(S, S_1, S_2, 0.001\right)$
$\begin{cases} S = \max\left(68.113\ 10^{-4}\exp(8.0613\ 10^{-3}\text{PremDepth}(P)), S\right) & \text{if } P \leq 13.71 \\ S = S_{\text{max}} & \text{if } P_{\text{cliff}} \leq P < 24 \\ S = S_{\text{LM}} & \text{if } P \geq 24 \end{cases}$
Basalt/Eclogite water solubility function
S_l=5.5; S_{l2}=4 S_{l3}=8
$S_1 = S_l(1 - \tanh((T - (770 + 40P))/200))/2$
$S_2 = S_{l2}\tanh((P - 7(T-900)/1000 - 2.8)/3.5)\exp(-(P-7)/12)$
$S_3 = S_{l3}\tanh((P - 8(T-1000)/1000 - 8)/1.5)$
$S = \max(S_1, S_2, S_3, 0.001)$
$\begin{cases} S = \max\left(68.113\ 10^{-4}\exp(8.0613\ 10^{-3}\text{PremDepth}(P)), S\right) & \text{if } P \leq 13.71 \\ S = S_{\text{LM}} & \text{if } P \geq 28 \end{cases}$
TTG water Solubility Function
S_l=3.4; S_{l2}=2 S_{l3}=3.7
$S_1 = S_l[(1 - \tanh((T - (770 + 10P))/100))/2]\ \exp(-P/50)$
$S_2 = S_{l2}\tanh((P - 5.9(T-900)/1000 - 2.8)/1.2)$
$S_3 = S_{l3}\tanh((P - 8(T-1000)/1000 - 8)/1.5)$
$S = \max(S_1, S_2, S_3, 0.001)$
$\begin{cases} S = \max\left(68.113\ 10^{-4}\exp(8.0613\ 10^{-3}\text{PremDepth}(P)), S\right) & \text{if } P \leq 13.71 \\ S = S_{\text{LM}} & \text{if } P \geq 28 \end{cases}$
Water solubility function of melts
$S = \max(\min(12P^{0.6} + P, 12\ 10^{0.6} + 10), 0.001)$

process is repeated until no more excess water exists in the mantle. If some excess water reaches the surface of the domain, it is then considered as erupted and is removed. This approach ensures that the water content in mantle rocks and melts remains acceptable.

Table B2. Function PremDepth gives depth (km) for pressure P (GPa).

Lower mantle
a = 3.11829162×10^{-6}; b = 0.0390269653; c = -P -3.56294332
$\begin{cases} depth = (P + 33.49617) / (0.058539) & \text{if } P \geq 126.95 \\ depth = \left(-b + \sqrt{b^2 - 4ac}\right) / (2a) & \text{if } P \geq 28.38 \\ depth = (P + 5.758207) / (0.04415793) & \text{if } P \geq 23.83 \end{cases}$
Transition zone
$\begin{cases} depth = (P + 2.875294) / (0.03985716) & \text{if } P \geq 21.02 \\ depth = (P + 2.056346) / (0.03845555) & \text{if } P \geq 13.32 \\ depth = (P + 0.5319232) / (0.03467901) & \text{if } P \geq 7.1 \end{cases}$
Lid
$\begin{cases} depth = (P + 0.213082) / (0.0332782) & \text{if } P \geq 0.6 \\ depth = (P) / \left(9.8 \cdot 2.6 \times 10^{-3}\right) & \text{if } P < 0.6 \end{cases}$

Appendix C: Calculating Magnesium number

The following calculations are done in the code only on tracers that fall under the protolith P-T conditions (Section 2.6) and then interpolated back to cell level. Knowing the P-T conditions on tracer level in our simulations, the expected MgO content in the melt is calculated by rearranging the empirical relationship (Eq. 1 of Lee and Chin (2014)) as:

$$\mathrm{MgO}^*_\mathrm{m} = \frac{T\left(P, \mathrm{MgO_m}, \mathrm{H_2O_m}\right) - 1070 - 72.23P + 3.249P^2 - 18.53\mathrm{H_2O}^*_\mathrm{m}}{14.93}, \tag{C1}$$

where T is the temperature (°C), P is the pressure (GPa), and $\mathrm{H_2O}^*_\mathrm{m}$ is the expected water concentration on the molten tracer. Following mass balance (Christensen and Hofmann, 1994), the expected MgO content in the residual tracer (solid harzburgite) is calculated as:

$$\mathrm{MgO}^*_\mathrm{r} = \frac{\mathrm{MgO_o} - \mathrm{MgO}^*_\mathrm{m} f}{(1 - f)}, \tag{C2}$$

where f is the mass fraction of the solid tracer that underwent melting, and $\mathrm{MgO_o}$ is the initial MgO concentration of the original solid tracer (unmelted peridotite, assuming a bulk silicate Earth value of 37.8 (McDonough and Sun, 1995)). The partition coefficient for MgO is calculated as:

$$D_\mathrm{MgO} = \frac{\mathrm{MgO}^*_\mathrm{r}}{\mathrm{MgO}^*_\mathrm{m}}. \tag{C3}$$

Next, the Fe-Mg equilibrium exchange between the peridotite and the melt is calculated following the empirical parameterisation of Herzberg and O'Hara (2002):

$$K_D = \frac{(\mathrm{FeO/MgO})_\mathrm{r}}{(\mathrm{FeO/MgO})_\mathrm{m}} = 0.381 - \frac{0.774}{\mathrm{MgO}^*_\mathrm{m}} + \frac{0.998}{\left(\mathrm{MgO}^*_\mathrm{m}\right)^2}. \tag{C4}$$

Knowing K_D and D_{MgO}, the partition coefficient for FeO follows as:

$$D_{\mathrm{FeO}} = K_D D_{\mathrm{MgO}}. \tag{C5}$$

Next, the actual partitioning of MgO and FeO is done and their concentrations on molten and solid tracers are updated as:

$$\mathrm{MgO_m} = \frac{\mathrm{MgO_o}}{D_{\mathrm{MgO}}(1-f)+f} \tag{C6}$$

$$\mathrm{MgO_r} = D_{\mathrm{MgO}}\mathrm{MgO_m}. \tag{C7}$$

Finally, the magnesium number on the residual solid tracer is updated as:

$$\mathrm{Mg\#} = \frac{\mathrm{MgO_r}/\mathrm{M_{MgO}}}{\mathrm{MgO_r}/\mathrm{M_{MgO}} + \mathrm{FeO_r}/\mathrm{M_{FeO}}}, \tag{C8}$$

where $\mathrm{M_{MgO}}$ and $\mathrm{M_{FeO}}$ are the molar masses (g/mol) of MgO (40.304) and FeO (71.844) respectively.

Appendix D: Crustal volume and mass of TTG

Based on Jain et al. (2019), the combined volume of basaltic and felsic crust at any given time t is given by:

$$V_{\text{crustal}}(t) = 4\pi\left[d_{\text{bas}}(t)\left(r_{\text{Earth}} - \frac{d_{\text{bas}}(t)}{2}\right)^2 + d_{\text{TTG}}(t)\left(r_{\text{Earth}} - \frac{d_{\text{TTG}}(t)}{2}\right)^2\right], \tag{D1}$$

with mean global basaltic crustal thickness at that time $d_{\text{bas}}(t)$, mean global TTG crustal thickness at that time $d_{\text{TTG}}(t)$, and the radius of Earth r_{Earth}. The volume of total TTG produced is given by:

$$V_{\text{TTG,total}}(t) = \frac{16 n_y}{\pi}\left(\frac{M_{\text{TTG,prod}}(t)}{\rho_{\text{s,TTG}}}\right), \tag{D2}$$

with number of cells in lateral direction n_y (512), mass of TTG produced $M_{\text{TTG,prod}}$ (code output). Here, a factor of 16 is applied to scale the mass of TTG produced from a quadrant annulus geometry to 3D Earth. The mass of TTG remaining is given by summing over all the cells i in the top 100 km of the computational domain:

$$M_{\text{TTG,rem}}(t) = \frac{16 n_y}{\pi}\rho_{\text{s,TTG}}\sum_i V_i C_{i,\text{TTG}}, \tag{D3}$$

where V_i is the cell volume and $C_{i\text{TTG}}$ is the dimensionless TTG concentration in the cell (ranging between 0 and 1).

Table E1. Cumulative global TTG mass and relative proportions of different TTG types.

Simulation	TTG mass (10^{22} kg)	Low P. (%)	Med. P. (%)	High P. (%)
A1	4.55	84.49	13.97	1.54
A2	3.67	82.59	15.36	2.05
A3	2.85	83.20	14.60	2.21
A4	2.84	81.14	15.95	2.91
A5	2.63	80.42	16.74	2.84
A6	3.60	84.39	13.85	1.76
A7	3.77	81.69	15.44	2.87
A8	2.42	75.10	20.16	4.74
A9	2.23	72.38	21.66	5.96
A10	1.92	69.28	23.04	7.67
A11	2.97	86.17	12.25	1.58
A12	2.57	81.17	15.45	3.38
A13	1.57	73.46	20.75	5.79
A14	2.33	74.86	20.16	4.98
A15	2.58	70.90	22.72	6.38
B1	1.94	67.99	24.11	7.90
B2	1.64	69.20	22.73	8.07
B3	1.45	71.28	20.88	7.85
B4	1.62	72.17	20.20	7.63
B5	1.53	72.47	20.35	7.17
B6	2.06	61.67	26.24	12.09
B7	1.82	64.19	23.69	12.12
B8	2.03	62.09	23.28	14.63
B9	1.99	65.22	21.53	13.25
B10	1.84	66.29	21.63	12.09
B11	2.55	63.20	21.63	15.17
B12	2.11	64.03	19.48	16.49
B13	2.33	63.29	20.11	16.60
B14	2.35	65.49	17.84	16.67
B15	2.24	66.60	17.57	15.84
C1	1.38	73.16	19.94	6.90
C2	2.44	74.69	18.36	6.95
C3	1.60	71.48	22.49	6.03
C4	1.59	71.83	21.15	7.02
C5	2.12	73.37	19.98	6.66
C6	1.67	70.66	19.00	10.34
C7	1.62	73.44	19.19	7.37
C8	1.51	72.52	19.98	7.50

Appendix E: Proportions of TTG

Author contributions. JVH conceptualised the study and outlined the research direction. JVH, CJ and ABR designed the set of numerical simulations. CJ ran the simulations and did post-processing. CJ and ABR produced the figures. ABR and AM developed the water/melting parameterisation and ABR coded it in StagYY. EJC helped with the Mg number parameterisation and CJ implemented it. All authors contributed to the article and approved the submitted version.

Competing interests. The authors declare no competing interests.

Acknowledgements. C. Jain and J. van Hunen were supported by the Natural Environment Research Council under the grant NE/M000281/1. C. Jain is also receiving funding from the ERC Synergy Grant 856555 for the project: Monitoring Earth Evolution through Time (MEET). A. Rozel is funded by ETH Zürich. We would like to thank James Connolly for his advice and for providing us with the water solubility. This work has made use of the facilities of ARCHER UK National Supercomputing Service (https://www.archer.ac.uk) and the Hamilton HPC Service of Durham University. The scientific colour map lapaz (Crameri, 2021) is used in this study to prevent visual distortion of the data and exclusion of readers with colour-vision deficiencies (Crameri et al., 2020).The StagPy library (Morison et al., 2021) and Paraview were used to process and visualise StagYY output data respectively.

References

Abe, Y.: Thermal Evolution and Chemical Differentiation of the Terrestrial Magma Ocean, in: Evolution of the Earth and Planets, vol. 90 of *Evolution of the Earth and Planets*, pp. 41 – 54, Evolution of the Earth and Planets, https://doi.org/10.1029/gm074p0041, http://doi.wiley.com/10.1029/GM074p0041, 1993a.

Abe, Y.: Physical state of the very early Earth, LITHOS, 30, 223 – 235, https://doi.org/10.1016/0024-4937(93)90037-d, http://linkinghub.elsevier.com/retrieve/pii/002449379390037D, 1993b.

Abe, Y.: Thermal and chemical evolution of the terrestrial magma ocean, Physics of the Earth and Planetary Interiors, 100, 27 – 39, https://doi.org/10.1016/s0031-9201(96)03229-3, http://linkinghub.elsevier.com/retrieve/pii/S0031920196032293, 1997.

Akaogi, M. and Navrotsky, A.: The quartz-coesite-stishovite transformations: new calorimetric measurements and calculation of phase diagrams, Physics of the Earth and Planetary Interiors, 36, 124–134, 1984.

Akimoto, S.-i. and Syono, Y.: Coesite-Stishovite transition, Journal of Geophysical Research, 74, 1653–1659, 1969.

Ammann, M. W., Brodholt, J. P., Wookey, J., and Dobson, D. P.: First-principles constraints on diffusion in lower-mantle minerals and a weak D" layer, Nature, 465, 462–465, 2010.

Andrault, D., Pesce, G., Bouhifd, M. A., Bolfan-Casanova, N., Henot, J.-M., and Mezouar, M.: Melting of subducted basalt at the core-mantle boundary, Science, 344, 892–895, 2014.

Armann, M. and Tackley, P. J.: Simulating the thermochemical magmatic and tectonic evolution of Venus's mantle and lithosphere: Two-dimensional models, Journal of Geophysical Research: Solid Earth (1978–2012), 117, 2012.

Arndt, N. T., Coltice, N., Helmstaedt, H., and Gregoire, M.: Origin of Archean subcontinental lithospheric mantle: Some petrological constraints, LITHOS, 109, 61–71, 2009.

Balay, S., Brown, J., Buschelman, K., Eijkhout, V., W. Gropp, D. K., Knepley, M., McInnes, L. C., Smith, B., and Zhang, H.: PETSc Users Manual, ANL-95/11 –Revision 3.3, 2012.

Beall, A. P., Moresi, L., and Cooper, C. M.: Formation of cratonic lithosphere during the initiation of plate tectonics, Geology, 46, 487–490, 2018.

Bercovici, D. and Ricard, Y.: Tectonic plate generation and two-phase damage: Void growth versus grain size reduction, Journal of Geophysical Research, 110, https://doi.org/10.1029/2004jb003181, 2005.

Bercovici, D. and Ricard, Y.: Plate tectonics, damage and inheritance, Nature, 508, 513 – 516, https://doi.org/10.1038/nature13072, http://www.nature.com/doifinder/10.1038/nature13072, 2014.

Boyd, F. R.: High-and low-temperature garnet peridotite xenoliths and their possible relation to the lithosphere-asthenosphere boundary beneath Africa, in: Mantle Xenolith, edited by Nixon, P. H., pp. 403–412, John Wiley & Sons Ltd., 1987.

Boyd, F. R.: Compositional distinction between oceanic and cratonic lithosphere, Earth and Planetary Science Letters, 96, 15–26, 1989.

Buffett, B. A., Huppert, H. E., Lister, J. R., and Woods, A. W.: Analytical Model for Solidification of the Earths Core, Nature, 356, 329–331, 1992.

Buffett, B. A., Huppert, H. E., Lister, J. R., and Woods, A. W.: On the thermal evolution of the Earth's core, Journal of Geophysical Research, 101, 7989–8006, 1996.

Byerlee, J.: Friction of Rocks, Pure and Applied Geophysics, 116, 615–626, 1978.

Canil, D.: Mildly incompatible elements in peridotites and the origins of mantle lithosphere, LITHOS, 77, 375–393, 2004.

Canil, D.: Canada's craton: A bottoms-up view, GSA today, 18, 4, 2008.

Capitanio, F. A., Nebel, O., and Cawood, P. A.: Thermochemical lithosphere differentiation and the origin of cratonic mantle, Nature, 588, 89–94, 2020.

Christensen, U. R.: Heat transport by variable viscosity convection and implications for the Earth's thermal evolution, Physics of the Earth and Planetary Interiors, 35, 264–282, https://doi.org/10.1016/0031-9201(84)90021-9, 1984.

Christensen, U. R. and Hofmann, A. W.: Segregation of subducted oceanic crust in the convecting mantle, Journal of Geophysical Research, 99, 19 867–19 884, 1994.

Čížková, H., van den Berg, A. P., Spakman, W., and Matyska, C.: The viscosity of Earth's lower mantle inferred from sinking speed of subducted lithosphere, Physics of the Earth and Planetary Interiors, 200-201, 56–62, 2012.

Connolly, J. A. D.: The geodynamic equation of state: What and how, Geochemistry, Geophysics, Geosystems, 10, https://doi.org/https://doi.org/10.1029/2009GC002540, 2009.

Crameri, F.: Scientific colour maps, https://doi.org/10.5281/zenodo.5501399, https://doi.org/10.5281/zenodo.5501399, 2021.

Crameri, F., Shephard, G. E., and Heron, P. J.: The misuse of colour in science communication, Nature Communications, 11, 5444, https://doi.org/10.1038/s41467-020-19160-7, 2020.

Crisp, J. A.: Rates of Magma Emplacement and Volcanic Output, Journal of Volcanology and Geothermal Research, 20, 177–211, 1984.

Debaille, V., O'Neill, C., Brandon, A. D., Haenecour, P., Yin, Q.-Z., Mattielli, N., and Treiman, A. H.: Stagnant-lid tectonics in early Earth revealed by 142Nd variations in late Archean rocks, Earth and Planetary Science Letters, 373, 83–92, 2013.

DeCelles, P. G., Ducea, M. N., Kapp, P., and Zandt, G.: Cyclicity in Cordilleran orogenic systems, Nature Geoscience, 2, 251–257, https://doi.org/10.1038/ngeo469, 2009.

Ducea, M. N. and Saleeby, J. B.: The age and origin of a thick mafic–ultramafic keel from beneath the Sierra Nevada batholith, Contributions to Mineralogy and Petrology, 133, 169–185, 1998.

Elkins-Tanton, L. T.: Magma Oceans in the Inner Solar System, Annual Review of Earth and Planetary Sciences, 40, 113 – 139, https://doi.org/10.1146/annurev-earth-042711-105503, http://www.annualreviews.org/doi/10.1146/annurev-earth-042711-105503, 2012.

Fischer, R. and Gerya, T.: Early Earth plume-lid tectonics: A high-resolution 3D numerical modelling approach, Journal of Geodynamics, 100, 198–214, 2016a.

Fischer, R. and Gerya, T.: Regimes of subduction and lithospheric dynamics in the Precambrian: 3D thermomechanical modelling, Gondwana Research, 37, 53 – 70, https://doi.org/10.1016/j.gr.2016.06.002, http://linkinghub.elsevier.com/retrieve/pii/S1342937X16301010, 2016b.

Gerya, T. V., Maresch, W. V., Podlesskii, K. K., and Perchuk, L. L.: Semi-empirical Gibbs free energy formulations for minerals and fluids for use in thermodynamic databases of petrological interest, Physics and Chemistry of Minerals, 31, 429–455, 2004.

Grand, S. P. and Helmberger, D. V.: Upper mantle shear structure of North America, Geophysical Journal International, 76, 399–438, 1984.

Grant, K., Ingrin, J., Lorand, J. P., and Dumas, P.: Water partitioning between mantle minerals from peridotite xenoliths, Contributions to Mineralogy and Petrology, 154, 15–34, https://doi.org/10.1007/s00410-006-0177-1, 2007.

Griffin, W. L. and O'Reilly, S. Y.: Cratonic lithospheric mantle: Is anything subducted?, Episodes, 30, 43–53, 2007.

Griffin, W. L., O'Reilly, S. Y., Abe, N., Aulbach, S., Davies, R. M., Pearson, N. J., Doyle, B. J., and Kivi, K.: The origin and evolution of Archean lithospheric mantle, Precambrian Research, 127, 19–41, 2003.

Guo, M. and Korenaga, J.: Argon constraints on the early growth of felsic continental crust, Science Advances, 6, https://doi.org/10.1126/sciadv.aaz6234, 2020.

Hall, C. E. and Parmentier, E. M.: Influence of grain size evolution on convective instability, Geochemistry, Geophysics, Geosystems, 4, 469, https://doi.org/10.1029/2002gc000308, http://doi.wiley.com/10.1029/2002GC000308, 2003.

Helmstaedt, H. and Schulze, D. J.: Southern African kimberlites and their mantle sample: Implications for Archean tectonics and lithosphere evolution, Journal of the Geological Society of Australia, 14, 358–368, 1989.

Hernlund, J. W. and Tackley, P. J.: Modeling mantle convection in the spherical annulus, Physics of the Earth and Planetary Interiors, 171, 48–54, 2008.

Herzberg, C. and O'Hara, M. J.: Plume-associated ultramafic magmas of phanerozoic age, Journal of Petrology, 43, 1857–1883, 2002.

Herzberg, C., Raterron, P., and Zhang, J.: New experimental observations on the anhydrous solidus for peridotite KLB-1, Geochemistry, Geophysics, Geosystems, 1, https://doi.org/https://doi.org/10.1029/2000GC000089, 2000.

Herzberg, C., Condie, K., and Korenaga, J.: Thermal history of the Earth and its petrological expression, Earth and Planetary Science Letters, 292, 79–88, 2010.

Herzberg, C. T.: Lithosphere peridotites of the Kaapvaal craton, Earth and Planetary Science Letters, 120, 13–29, 1993.

Hickman, A. H.: Two contrasting granite-greenstone terranes in the Pilbara Craton, Australia: evidence for vertical and horizontal tectonic regimes prior to 2900Ma, Precambrian Research, 131, 153–172, 2004.

Hirschmann, M. M.: Water, Melting, and the Deep Earth H_2O Cycle, Annual Review of Earth and Planetary Sciences, 34, 629–653, 2006.

Hirth, G. and Kohlstedt, D. L.: Water in the oceanic upper mantle: implications for rheology, melt extraction and the evolution of the lithosphere, Earth and Planetary Science Letters, 144, 93–108, 1996.

Hirth, G., Evans, R. L., and Chave, A. D.: Comparison of continental and oceanic mantle electrical conductivity: Is the Archean lithosphere dry?, Geochemistry, Geophysics, Geosystems, 1, n/a–n/a, 2000.

Hunt, S. A., Weidner, D. J., Li, L., Wang, L., Walte, N. P., Brodholt, J. P., and Dobson, D. P.: Weakening of calcium iridate during its transformation from perovskite to post-perovskite, Nature Geoscience, 2, 794–797, 2009.

Irifune, T. and Ringwood, A. E.: Phase-Transformations in Subducted Oceanic-Crust and Buoyancy Relationships at Depths of 600-800 Km in the Mantle, Earth and Planetary Science Letters, 117, 101–110, 1993.

Jain, C., Rozel, A. B., Tackley, P. J., Sanan, P., and Gerya, T. V.: Growing primordial continental crust self-consistently in global mantle convection models, Gondwana Research, 73, 96–122, 2019.

Jin, Z. M., Zhang, J., Green II, H. W., and Jin, S.: Eclogite rheology: Implications for subducted lithosphere, Geology, 29, 667, 2001.

Jordan, T. H.: Composition and development of the continental tectosphere, Nature, 274, 544–548, 1978.

Jordan, T. H.: Mineralogies, densities and seismic velocities of garnet lherzolites and their geophysical implications, in: The Mantle Sample: Inclusion in Kimberlites and Other Volcanics, pp. 1–14, American Geophysical Union, Washington, D. C., 1979.

Jordan, T. H.: Structure and Formation of the Continental Tectosphere, Journal of Petrology, Special Volume, 11–37, 1988.

Karato, S.: Water in the Evolution of the Earth and Other Terrestrial Planets, in: Treatise on Geophysics: Second Edition, pp. 105–144, Elsevier, 2015.

Karato, S. i. and Wu, P.: Rheology of the Upper Mantle: A Synthesis, Science, 260, 771–778, 1993.

Kay, S. M., Godoy, E., and Kurtz, A.: Episodic arc migration, crustal thickening, subduction erosion, and magmatism in the south-central Andes, Geological Society of America Bulletin, 117, 67, https://doi.org/10.1130/b25431.1, https://pubs.geoscienceworld.org/gsabulletin/article/117/1-2/67-88/2143, 2005.

Kelemen, P. B., Hart, S. R., and Bernstein, S.: Silica enrichment in the continental upper mantle via melt/rock reaction, Earth and Planetary Science Letters, 164, 387–406, 1998.

Kessel, R., Pettke, T., and Fumagalli, P.: Melting of metasomatized peridotite at 4–6 GPa and up to 1200 °C: an experimental approach, Contributions to Mineralogy and Petrology, 169, 37, https://doi.org/10.1007/s00410-015-1132-9, https://doi.org/10.1007/s00410-015-1132-9, 2015.

King, S.: Archean cratons and mantle dynamics, Earth and Planetary Science Letters, 234, 1 – 14, https://doi.org/10.1016/j.epsl.2005.03.007, http://linkinghub.elsevier.com/retrieve/pii/S0012821X05001895, 2005.

Korenaga, J.: Initiation and Evolution of Plate Tectonics on Earth: Theories and Observations, Annual Review of Earth and Planetary Sciences, 41, 117–151, 2013.

Korenaga, J.: Hadean geodynamics and the nature of early continental crust, Earth and Planetary Science Letters, https://doi.org/10.1016/j.precamres.2021.106178, 2021.

Lee, C.-T. A.: Compositional variation of density and seismic velocities in natural peridotites at STP conditions: Implications for seismic imaging of compositional heterogeneities in the upper mantle, Journal of Geophysical Research, 108, 589, 2003.

Lee, C.-T. A. and Chin, E. J.: Calculating melting temperatures and pressures of peridotite protoliths: Implications for the origin of cratonic mantle, Earth and Planetary Science Letters, 403, 273–286, 2014.

Lee, C.-T. A., Luffi, P., Höink, T., Li, Z.-X. A., and Lenardic, A.: The role of serpentine in preferential craton formation in the late Archean by lithosphere underthrusting, Earth and Planetary Science Letters, 269, 96–104, 2008.

Lee, C.-T. A., Luffi, P., and Chin, E. J.: Building and Destroying Continental Mantle, Annual Review of Earth and Planetary Sciences, 39, 59–90, 2011.

Lenardic, A. and Moresi, L. N.: Some thoughts on the stability of cratonic lithosphere: Effects of buoyancy and viscosity, Journal of Geophysical Research, 104, 12 747–12 758, 1999.

Lenardic, A., Moresi, L. N., and Muhlhaus, H.: Longevity and stability of cratonic lithosphere: Insights from numerical simulations of coupled mantle convection and continental tectonics, Journal of Geophysical Research: Solid Earth, 108, 2003.

Li, Z.-X. A., Lee, C.-T. A., Peslier, A. H., Lenardic, A., and Mackwell, S. J.: Water contents in mantle xenoliths from the Colorado Plateau and vicinity: Implications for the mantle rheology and hydration-induced thinning of continental lithosphere, Journal of Geophysical Research, 113, 963, https://doi.org/10.1029/2007jb005540, http://doi.wiley.com/10.1029/2007JB005540, 2008.

Litasov, K. and Ohtani, E.: Phase relations and melt compositions in CMAS–pyrolite–H2O system up to 25 GPa, Physics of the Earth and Planetary Interiors, 134, 105–127, https://doi.org/https://doi.org/10.1016/S0031-9201(02)00152-8, 2002.

Lourenço, D. L., Rozel, A., and Tackley, P. J.: Melting-induced crustal production helps plate tectonics on Earth-like planets, Earth and Planetary Science Letters, 439, 18–28, 2016.

Lourenço, D. L., Rozel, A. B., Ballmer, M. D., and Tackley, P. J.: Plutonic-Squishy Lid: A New Global Tectonic Regime Generated by Intrusive Magmatism on Earth-Like Planets, Geochemistry, Geophysics, Geosystems, 21, B01 412, https://doi.org/10.1029/2019gc008756, https://onlinelibrary.wiley.com/doi/abs/10.1029/2019GC008756, 2020.

Luffi, P., Saleeby, J. B., Lee, C.-T. A., and Ducea, M. N.: Lithospheric mantle duplex beneath the central Mojave Desert revealed by xenoliths from Dish Hill, California, Journal of Geophysical Research, 114, 375, 2009.

Maaløe, S.: The solidus of harzburgite to 3 GPa pressure: the compositions of primary abyssal tholeiite, Mineralogy and Petrology, 81, 1–17, https://doi.org/https://doi.org/10.1007/s00710-004-0028-6, 2004.

McDonough, W. F. and Sun, S. S.: The composition of the Earth, Chemical geology, 120, 223–253, 1995.

Mondal, P. and Korenaga, J.: A propagator matrix method for the Rayleigh–Taylor instability of multiple layers: a case study on crustal delamination in the early Earth, academic.oup.com, https://doi.org/10.1093/gji/ggx513, https://academic.oup.com/gji/article-abstract/212/3/1890/4675221, 2018.

Moore, W. B. and Webb, A. A. G.: Heat-pipe Earth, Nature, 501, 501–505, 2014.

Moresi, L. and Solomatov, V.: Mantle convection with a brittle lithosphere: thoughts on the global tectonic styles of the Earth and Venus, Geophysical Journal International, 133, 669–682, 1998.

Morison, A., Ulvrova, M., Labrosse, S., B4rsh, theofatou, and tfrass49: StagPython/StagPy:, https://doi.org/10.5281/zenodo.5512349, https://doi.org/10.5281/zenodo.5512349, 2021.

Moyen, J.-F.: The composite Archaean grey gneisses: Petrological significance, and evidence for a non-unique tectonic setting for Archaean crustal growth, LITHOS, 123, 21–36, 2011.

Moyen, J.-F. and Laurent, O.: Archaean tectonic systems: A view from igneous rocks, Lithos, 302-303, 99–125, https://doi.org/10.1016/j.lithos.2017.11.038, 2018.

Nakagawa, T. and Tackley, P. J.: Effects of thermo-chemical mantle convection on the thermal evolution of the Earth's core, Earth and Planetary Science Letters, 220, 107–119, 2004.

Nakagawa, T. and Tackley, P. J.: Influence of magmatism on mantle cooling, surface heat flow and Urey ratio, Earth and Planetary Science Letters, 329, 1–10, 2012.

Nakagawa, T., Tackley, P. J., Deschamps, F., and Connolly, J. A. D.: The influence of MORB and harzburgite composition on thermo-chemical mantle convection in a 3-D spherical shell with self-consistently calculated mineral physics, Earth and Planetary Science Letters, 296, 403–412, 2010.

Noack, L., Breuer, D., and Spohn, T.: Coupling the atmosphere with interior dynamics: Implications for the resurfacing of Venus, Icarus, 217, 484–498, https://doi.org/10.1016/j.icarus.2011.08.026, 2012.

Nyblade, A. A.: Heat flow and the structure of Precambrian lithosphere, Developments in Geotectonics, 24, 81–91, 1999.

O'Neill, C. J., Lenardic, A., Griffin, W. L., and O'Reilly, S. Y.: Dynamics of cratons in an evolving mantle, LITHOS, 102, 12–24, 2008.

Ono, S., Ito, E., and Katsura, T.: Mineralogy of subducted basaltic crust (MORB) from 25 to 37 GPa, and chemical heterogeneity of the lower mantle, Earth and Planetary Science Letters, 190, 57–63, 2001.

Palin, R. M. and Santosh, M.: Plate tectonics: What, where, why, and when?, Gondwana Research, https://doi.org/10.1016/j.gr.2020.11.001, https://linkinghub.elsevier.com/retrieve/pii/S1342937X20302847, 2020.

Parman, S. W.: A subduction origin for komatiites and cratonic lithospheric mantle, South African Journal of Geology, 107, 107–118, 2004.

Pearson, D. G. and Wittig, N.: Formation of Archaean continental lithosphere and its diamonds: the root of the problem, Journal of the Geological Society, 165, 895–914, 2008.

Pearson, D. G., Scott, J. M., Liu, J., Schaeffer, A., Wang, L. H., Hunen, J. v., Szilas, K., Chacko, T., and Kelemen, P. B.: Deep continental roots and cratons., Nature, 596, 199–210, https://doi.org/10.1038/s41586-021-03600-5, 2021.

Perchuk, A. L., Gerya, T. V., Zakharov, V. S., and Griffin, W. L.: Building cratonic keels in Precambrian plate tectonics, Nature, 586, 395–401, 2020.

Pertermann, M. and Hirschmann, M. M.: Partial melting experiments on a MORB-like pyroxenite between 2 and 3 GPa: Constraints on the presence of pyroxenite in basalt source regions from solidus location and melting rate, Journal of Geophysical Research: Solid Earth, 108, https://doi.org/https://doi.org/10.1029/2000JB000118, 2003.

Peslier, A. H.: A review of water contents of nominally anhydrous natural minerals in the mantles of Earth, Mars and the Moon, Journal of Volcanology and Geothermal Research, 197, 239–258, https://doi.org/10.1016/j.jvolgeores.2009.10.006, 2010.

Pollack, H. N.: Cratonization and thermal evolution of the mantle, Earth and Planetary Science Letters, 80, 175–182, 1986.

Pollack, H. N., Hurter, S. J., and Johnson, J. R.: Heat flow from the Earth's interior: Analysis of the global data set, Reviews of Geophysics, 31, 267–280, 1993.

Ricard, Y. and Bercovici, D.: A continuum theory of grain size evolution and damage, Journal of Geophysical Research: Solid Earth, 114, https://doi.org/10.1029/2007jb005491, 2009.

Rozel, A., Ricard, Y., and Bercovici, D.: A thermodynamically self-consistent damage equation for grain size evolution during dynamic recrystallization, Geophysical Journal International, 184, 719–728, 2011.

Rozel, A., Golabek, G. J., Näf, R., and Tackley, P. J.: Formation of ridges in a stable lithosphere in mantle convection models with a viscoplastic rheology, Geophysical Research Letters, 42, 4770–4777, https://doi.org/10.1002/2015gl063483, 2015.

Rozel, A. B., Golabek, G. J., Jain, C., Tackley, P. J., and Gerya, T.: Continental crust formation on early Earth controlled by intrusive magmatism, Nature, 545, 332–335, 2017.

Saleeby, J.: Segmentation of the Laramide Slab—evidence from the southern Sierra Nevada region, Geological Society of America Bulletin, 115, 655–668, 2003.

Schulze, D. J.: Constraints on the abundance of eclogite in the upper mantle, Journal of Geophysical Research, 94, 4205–4212, 1989.

Schutt, D. L. and Lesher, C. E.: Effects of melt depletion on the density and seismic velocity of garnet and spinel lherzolite, Journal of Geophysical Research, 111, n/a–n/a, 2006.

Şengör, A. M. C., Natal'in, B. A., and Burtman, V. S.: Evolution of the Altaid tectonic collage and Palaeozoic crustal growth in Eurasia, Nature, 364, 299–307, 1993.

Simon, N. S. C., Carlson, R. W., Pearson, D. G., and Davies, G. R.: The Origin and Evolution of the Kaapvaal Cratonic Lithospheric Mantle, Journal of Petrology, 48, 589–625, 2007.

Sizova, E., Gerya, T., Brown, M., and Perchuk, L. L.: Subduction styles in the Precambrian: Insight from numerical experiments, LITHOS, 116, 209–229, 2010.

Sleep, N. H.: Survival of Archean cratonal lithosphere, Journal of Geophysical Research, 108, 2003.

Solomatov, V. S.: Scaling of Temperature-Dependent and Stress-Dependent Viscosity Convection, Physics of Fluids, 7, 266 – 274, https://doi.org/10.1063/1.868624, http://scitation.aip.org/content/aip/journal/pof2/7/2/10.1063/1.868624, 1995.

Stein, C., Schmalzl, J., and Hansen, U.: The effect of rheological parameters on plate behaviour in a self-consistent model of mantle convection, Physics of the Earth and Planetary Interiors, 142, 225–255, https://doi.org/10.1016/j.pepi.2004.01.006, 2004.

Tackley, P. J.: Self-consistent generation of tectonic plates in time-dependent, three-dimensional mantle convection simulations 1. Pseudo-plastic yielding, Geochemistry, Geophysics, Geosystems, 1, n/a – n/a, https://doi.org/10.1029/2000gc000036, https://www.scopus.com/inward/record.uri?partnerID=HzOxMe3b&scp=84882842780&origin=inward, 2000.

Tackley, P. J.: Modelling compressible mantle convection with large viscosity contrasts in a three-dimensional spherical shell using the yin-yang grid, Physics of the Earth and Planetary Interiors, 171, 7–18, 2008.

Tackley, P. J., Ammann, M., Brodholt, J. P., Dobson, D. P., and Valencia, D.: Mantle dynamics in super-Earths: Post-perovskite rheology and self-regulation of viscosity, Icarus, 225, 50–61, 2013.

Turcotte, D. L.: An episodic hypothesis for Venusian tectonics, Journal of Geophysical Research, 98, 17 061, https://doi.org/10.1029/93je01775, 1993.

Van Kranendonk, M. J.: Cool greenstone drips and the role of partial convective overturn in Barberton greenstone belt evolution, Journal of African Earth Sciences, 60, 346–352, 2011.

Van Kranendonk, M. J., Collins, W. J., Hickman, A., and Pawley, M. J.: Critical tests of vertical vs. horizontal tectonic models for the Archaean East Pilbara Granite–Greenstone Terrane, Pilbara Craton, Western Australia, Precambrian Research, 131, 173–211, 2004.

Wang, H., van Hunen, J., Pearson, D. G., and Allen, M. B.: Craton stability and longevity: The roles of composition-dependent rheology and buoyancy, Earth and Planetary Science Letters, 391, 224–233, 2014.

Wang, H., van Hunen, J., and Pearson, D. G.: Making Archean cratonic roots by lateral compression: A two-stage thickening and stabilization model, Tectonophysics, 746, 562–571, 2018.

Xie, S. and Tackley, P. J.: Evolution of U-Pb and Sm-Nd systems in numerical models of mantle convection and plate tectonics, Journal of Geophysical Research, 109, 2004.

Xu, W., Lithgow-Bertelloni, C., Stixrude, L., and Ritsema, J.: The effect of bulk composition and temperature on mantle seismic structure, Earth and Planetary Science Letters, 275, 70–79, 2008.

Yamazaki, D. and Karato, S.-i.: Some mineral physics constraints on the rheology and geothermal structure of Earth's lower mantle, American Mineralogist, 86, 385–391, 2001.

Yang, X.-Z., Xia, Q.-K., Deloule, E., Dallai, L., Fan, Q.-C., and Feng, M.: Water in minerals of the continental lithospheric mantle and overlying lower crust: A comparative study of peridotite and granulite xenoliths from the North China Craton, Chemical Geology, 256, 33–45, https://doi.org/10.1016/j.chemgeo.2008.07.020, 2008.

Zerr, A., Diegeler, A., and Boehler, R.: Solidus of Earth's deep mantle, Science, 281, 243–246, 1998.